Angewandte Chemie

Eine Zeitschrift der Gesellschaft Deutscher Chemiker

Supporting Information

Binuclear Copper(I) Complexes for Near-Infrared Light-Emitting Electrochemical Cells

A. Jouaiti*, L. Ballerini, H.-L. Shen, R. Viel, F. Polo, N. Kyritsakas, S. Haacke, Y.-T. Huang, C.-W. Lu, C. Gourlaouen, H.-C. Su*, M. Mauro*

Supporting Information

Table of Contents

Supplementary experimental methods

General consideration

5-Bromopicolinaldehyde, (3,5-di-tert-butylphenyl)boronic acid, dithiooxamide, oxy-di-2,1-phenylene)bis(diphenylphosphine) (DPEPhos) and 9,9-dimethyl-9H-xanthene-4,5-diyl)bis(diphenylphosphine) (Xantphos) are commercially available and were used as received. Solvents and other commonly available reagents were purchased and used without further purification. 2-(5-Bromopyridin-2-yl)-1,3-benzothiazole (**1**) was synthesized as reported in literature.[27] Silica gel for column chromatography was purchased from Sigma-Aldrich. ^{1}H, ^{13}C{^{1}H} and ^{31}P{^{1}H} NMR spectra were recorded at 298 K on either Bruker AV500 spectrometer in deuterated solvents and the residual solvent peak was used as the internal reference. All the chemical shifts (δ) are reported in ppm. High-resolution electrospray mass spectrometry (HR-ESI-MS) was performed by the Service Spectrométrie de Masse of the Fédération de Chimie "Le Bel" FR2010 of the University of Strasbourg. Experimental NMR and MS spectra are available in the Supporting Information.

Synthesis

2-(5-(3,5-di-*tert*-butylphenyl)pyridin-2-yl)benzo[*d*]thiazole (L2). A mixture of 2-(5-bromopyridin-2-yl)-1,3-benzothiazole (0.5 g, 1.7 mmol), Na_2CO_3 (0.55 g, 4.7 mmol) and (3,5-di-tert-butylphenyl)boronic acid (0.52g, 2.2 mmol) in 28 mL of a mixture 1,4-dioxane/H_2O (3:1 v/v) was degassed by steady bubbling with argon for 20 minutes. Pd(PPh$_3$)$_4$ (0.02 g, 0.018 mmol) was added, and the mixture was refluxed for 7 hours under argon. After cooling the mixture, it was extracted with CH_2Cl_2 (3×40 mL). The combined organic layers were washed with brine, dried over $MgSO_4$ and evaporated under vacuum. The residue was purified by silica gel column chromatography with petroleum ether/CH_2Cl_2 mixture varying from 100:0 to 50:50 as eluent to provide the target compound **2** as a white solid (0.6 g, yield 87%). ^{1}H NMR (CDCl$_3$, 500 MHz) δ: 8.97 (d, 1H, J = 5 Hz), 8.47 (d, J = 10 Hz, 1H), 8.15 (d, 1H, J = 10 Hz), 8.07 (dd, J = 5 Hz, J = 10 Hz, 1H), 7.97 (d, 1H, J = 10 Hz), 7.56–7.44 (m, 5H), 1.43 (s, 18 H). ^{13}C NMR (CDCl$_3$, 125 MHz) δ: 169.3, 154.3, 151.8, 149.7, 148.3, 139.4, 136.5, 136.1, 135.4, 126.3, 125.6, 123.5, 122.8, 122.0, 121.6, 120.6, 35.1, 31.5. HR-MS (ESI): m/z [M + H]$^+$ calcd for C$_{26}$H$_{29}$N$_2$S [M + H]$^+$ 401.2046, found 401.2047.

5-(3,5-di-*tert*-butylphenyl)picolinaldehyde (2). A mixture of 5-bromopicolinaldehyde (1.0 g, 5.3 mmol), (3,5-di-*tert*-butylphenyl)boronic acid (1.51 g, 6.4 mmol) and K_2CO_3 (1.48 g, 10.7 mmol) in 20 mL of DMF was degassed by steady bubbling with argon for 20 minutes. Pd(PPh$_3$)$_4$ (0.02 g, 0.018 mmol) was added to the mixture and this latter was allowed to stir for 24 hours

at 90°C under an argon atmosphere. After, the mixture was evaporated to dryness under reduced pressure and extracted with CH_2Cl_2 (2×50 mL). The combined organic layers were washed with brine, dried over $MgSO_4$ and evaporated under vacuum. The residue was purified by silica gel column chromatography with CH_2Cl_2/petroleum ether mixture varying from 50:50 to 100:0 as eluent to provide the target compound **3** as a white solid (0.6 g, yield 38%). ^1H NMR (CDCl$_3$, 500 MHz) δ: 10.12 (s, 1H), 8.98 (s, 1H), 8.02 (s, 2H), 7.53 (d, J = 2 Hz, 1H), 7.42 (d, J = 2Hz, 2H), 1.37 (s, 18H). ^{13}C NMR (CDCl$_3$, 125 MHz) δ: 193.1, 152.0, 151.2, 148.9, 142.0, 136.0, 135.5, 123.4, 121.9, 121.8, 35.1, 31.5. HR-MS (ESI): m/z [M + H]$^+$ calcd for $C_{20}H_{26}NO$ [M + H]$^+$ 296.2009, found 296.2000.

2,5-*bis*(5-(3,5-di-*tert*-butylphenyl)pyridin-2-yl)thiazolo[5,4-*d*]thiazole (L1). Compound **2** (0.50 g, 1.7 mmol) and dithiooxamide (0.10 g, 0.83 mmol) were dissolved in 15 mL of DMF and the resulting mixture was refluxed overnight under an argon atmosphere. The reaction mixture was cooled down to room temperature and the desired compound **L1** was obtained as a yellow precipitate upon filtration. The solid was washed with MeOH and dried under vacuum (0.35 g, yield 62%). Yellow crystals were obtained by slow evaporation of CH_2Cl_2/EtOH solution. ^1H NMR (CDCl$_3$, 500 MHz) δ: 8.89 (d, , J = 2 Hz, 2H), 8.29 (d, J = 8.5 Hz, 2H), 8.03 (dd, J = 2 Hz, J = 8.5 Hz, 2H), 7.51 (s, J = 10 Hz, 2H); 7.46 (d, J = 2 Hz, 4H); 1.38 (s, 36H). ^{13}C NMR (CDCl$_3$, 125 MHz) δ: 170.5, 153.4, 151.9, 149.7, 148.3, 139.2, 136.4, 135.6, 122.9, 121.5, 119.8, 35.1, 31.5. HR-MS (ESI): m/z [M + H]$^+$ calcd for $C_{42}H_{49}N_4S_2$ [M + H]$^+$ 673.3393, found 673.3396.

[Cu(DPEPhos)(L2)]PF$_6$ (M1). Under a stream of argon, [Cu(CH$_3$CN)$_4$]PF$_6$ (104 mg, 0.28 mmol) was added to a 15 mL DCM stirred solution containing DPEPhos (150 mg, 0.28 mmol) at room temperature. After 5 minutes, compound **L2** (0.111 mg, 0.277 mmol) was added and the mixture was stirred for 4 hours at room temperature. The orange mixture was almost evaporated to dryness under reduced pressure and diethyl ether was added, gave an orange powder. The complex was obtained by filtration, washed with diethyl ether and dried (0.175 g, 63% yield). The single crystals for X-ray structural analysis were obtained by slow diffusion of cyclohexane into the CHCl$_3$ solution of the complexes. ^1H NMR (CDCl$_3$, 500 MHz) δ: 8.48 (s, 1H), 8.24 (d, J = 5 Hz, 2H), 7.98 (d, J = 10 Hz, 1H), 7.68 (d, J = 10 Hz, 1H), 7.55 (t, J = 5 Hz, 1H), 7.45 (td, J = 5 Hz, J = 10 Hz, 1H), 7.31-7.26 (m, 5H), 7.22 (t, J = 10 Hz, 2H), 7.16-7.12 (m, 10H), 7.10-7.00 (m, 12H), 6.92-6.89 (m, 2H), 1.40 (s, 18H). ^{13}C NMR (CDCl$_3$, 125 MHz) δ: 164.8, 158.3 (t, $J_{P\text{-}C}$ = 10 Hz), 152.0, 150.0, 147.8, 146.1, 141.1, 137.1, 134.7, 134.5, 134.2, 133.1 (t, $J_{P\text{-}C}$ = 7.5 Hz), 132.7 (t, $J_{P\text{-}C}$ = 7.5 Hz), 131.4, 132.2, 130.6 (t, $J_{P\text{-}C}$ = 17.6 Hz), 130.4, 130.3 (t, $J_{P\text{-}C}$ = 17.6 Hz), 130.2, 130.1, 128.8 (dt, $J_{P\text{-}C}$ = 5 Hz, $J_{P\text{-}C}$ = 15 Hz), 127.5, 127.2, 125.3,

124.7, 123.9 6 (t, J_{P-C} = 15 Hz), 123.6, 122.8, 122.3, 121.4, 120.2, 35.0, 31.4. ^{31}P NMR (121.5 MHz, CDCl$_3$) δ: −11.5 (broad), −143.9 (sep, $^1J_{P-F}$ = 708 Hz). HR-MS (ESI): m/z [M]$^+$ calcd for C$_{62}$H$_{56}$CuN$_2$OP$_2$S 1001.2879, found 1001.2873.

[Cu(xantphos)(L2)]PF$_6$ (M2). This compound was prepared by a synthetic procedure similar to that of **[Cu(DPEPhos)(L2)]PF$_6$** except for using xantphos instead of DPEPhos. Color: orange, 0.160 g, yield 60%. The single crystals for X-ray structural analysis were obtained by slow diffusion of diethyl ether into the CHCl$_3$ solution of the complexes. ^{1}H NMR (CDCl$_3$, 500 MHz) δ: 8.74 (s, 1H), 8.28 (s, 2H), 8.02 (d, J = 5 Hz, 1H), 7.70 (d, J = 5 Hz, 2H), 7.57 (s, 1H), 7.40–7.30 (m, 3H), 7.30–7.15 (m, 14H), 7.05–7.15 (m, 4H), 6.95–6.87 (m, 1H), 6.75–6.79 (m, 4H), 6.67–6.60 (m, 3H), 1.99, (s, 3H), 1.64 (s, 3H), 1.39 (s, 18H). ^{13}C NMR (CDCl$_3$, 125 MHz) δ: 165.2, 155.0 (t, J_{P-C} = 10 Hz), 152.3, 149.9.0, 147.5, 146.0, 141.2, 137.4, 134.9, 134.6, 133.9, 132.9 (t, J_{P-C} = 7.5 Hz), 132.5 (t, J_{P-C} = 7.5 Hz), 131.4 (t, J_{P-C} = 16 Hz), 131.2, 131.0 (t, J_{P-C} = 16 Hz), 130.3, 130.0, 129.0, 128.9, 128.8, 127.4, 127.3, 123.8, 123.2, 121.4, 120.0 (t, J_{P-C} = 16 Hz), 36.2 35.1, 31.4, 31.1, 25.8. ^{31}P NMR (121.5 MHz, CDCl$_3$) δ: −11.5 (broad), −143.9 (sep, $^1J_{P-F}$ = 708 Hz). HR-MS (ESI): m/z [M]$^+$ calcd for C$_{65}$H$_{60}$CuN$_2$OP$_2$S 1041.3192, found 1041.3204.

[Cu$_2$(DPEPhos)$_2$(L1)](PF$_6$)$_2$ (Cu-NIR1). Under a stream of argon, [Cu(CH$_3$CN)$_4$]PF$_6$ (69 mg, 0.18 mmol) was added to a 15 mL DCM stirred solution containing DPEPhos (100 mg, 0.18 mmol) at room temperature. After 5 minutes, compound **L1** (62 mg, 0.09 mmol) was added and the mixture was stirred for 4 h at room temperature. The red mixture was almost evaporated to dryness under reduced pressure and diethyl ether was added, it gave a red powder. The complex was obtained by filtration, washed with diethyl ether and dried (0.2 g, 59% yield). The single crystals for X-ray structural analysis were obtained by slow diffusion of diethylether into the CH$_2$Cl$_2$ solution of the complexes. ^{1}H NMR (CDCl$_3$, 500 MHz) δ: 8.47 (s, 2H), 8.28 (d, J = 8 Hz, 2H), 8.15 (d, J = 8 Hz, 2H), 7.56 (s, 2H), 7.37 (t, J = 8 Hz, 4H), 7.26 (t, J = 8 Hz, 4H), 7.22-6.96 (m, 48H), 6.72-6.78 (m, 4H), 1.37 (s, 36H). ^{13}C NMR (CDCl$_3$, 125 MHz) δ: 167.6, 158.3 (t, J_{P-C} = 6 Hz), 152.2, 150.2, 148.4, 144.9, 142.1, 137.5, 134.6, 134.4, 133.2 (t, J_{P-C} = 7.5 Hz), 132.9 (t, J_{P-C} = 7.5 Hz), 132.5, 130.5, 130.4, 130.2 (d, J_{P-C} = 5.6 Hz), 130.1 (d, J_{P-C} = 5.6 Hz), 125.4, 124.0, 123.9, 123.1, 123.2, 123.1, 122.9, 121.5, 120.7, 35.0, 31.1. ^{31}P NMR (121.5 MHz, CDCl$_3$) δ: −11.6 (broad), −143.9 (sep, $^1J_{P-F}$ = 708 Hz). HR-MS (ESI): m/z [M + PF$_6$]$^+$ calcd for C$_{114}$H$_{105}$Cu$_2$F$_6$N$_4$O$_2$P$_5$S$_2$, 2019.4779, found 2019.4734.

[Cu$_2$(xantphos)$_2$(L1)](PF$_6$)$_2$ (Cu-NIR2). This compound was prepared by a synthetic procedure similar to that of **[Cu$_2$(DPEPhos)$_2$(L1)](PF$_6$)$_2$** except for using xantphos instead of DPEPhos. Color: red, 0.19 g, yield 57%. The single crystals for X-ray structural analysis were

obtained by slow diffusion of diethyl ether into the CH_2Cl_2 solution of the complexes. ^1H NMR (CDCl$_3$, 500 MHz) δ: 8.58 (s, 2H), 8.33 (d, J = 8 Hz, 2H), 7.87 (d, J = 8 Hz, 4H), 7.67 (d, J = 8 Hz, 2H), 7.55 (s, 2H), 7.22–7.28 (m, 12H), 7.16 (s, 4H), 7.00–7.07 (m, 24H), 6.80–6.84 (m, 8H), 6.66–6.80 (m, 4H), 1.94, (s, 6H), 1.70 (s, 6H), 1.32 (s, 36H). ^{13}C NMR (CDCl$_3$, 125 MHz) δ: 167.6, 155.0 (t, J_{P-C} = 6 Hz), 152.4, 149.7, 148.1, 144.4, 142.4, 137.9, 134.5, 134.2, 132.9 (t, J_{P-C} = 7.5 Hz), 132.3 (t, J_{P-C} = 7.5 Hz), 131.3, 130.7, 130.6, 130.4, 130.5, 130.2, 129.1 (d, J_{P-C} = 17.7 Hz), 128.2, 125.6, 124.2, 123.5, 121.5, 121.5, 119.4, 119.2, 119.1, 36.2, 34.9, 31.1, 29.6, 27.0. ^{31}P NMR (121.5 MHz, CDCl$_3$) δ: −11.5 (broad), −143.9 (sep, $^1J_{P-F}$ = 708 Hz) HR-MS (ESI): m/z [M + PF$_6$]$^+$ calcd for $C_{120}H_{112}Cu_2F_6N_4O_2P_5S_2$, 2099.5405, found 2099.5405.

X-ray crystallographic analysis

The crystals were placed in oil, and a single crystal was selected, mounted on a glass fibre and placed in a low-temperature N$_2$ stream. X-ray diffraction data collection was carried out on a Bruker PHOTON III DUO CPAD diffractometer equipped with an Oxford Cryosystem liquid N$_2$ device, using Mo-Kα radiation (λ = 0.71073 Å). The crystal-detector distance was 38mm. The cell parameters were determined (APEX3 software) [28] from reflections taken from 1 set of 180 frames at 1s exposure. The structure was solved using the program SHELXT-2014[29]. The refinement and all further calculations were carried out using SHELXL-2018[30]. The other H-atoms were included in calculated positions and treated as riding atoms using SHELXL default parameters. The non-H atoms were refined anisotropically, using weighted full-matrix least-squares on F^2. A semi-empirical absorption correction was applied using SADABS in APEX3[28]; transmission factors: T$_{min}$/T$_{max}$ = 0.6820 /0.7456

Photophysical measurements

Steady-state emission spectra were recorded on a Horiba Jobin−Yvon IBH FL-322 Fluorolog 3 spectrometer equipped with a 450 W xenon arc lamp, double-grating excitation, and emission monochromators (2.1 nm mm$^{−1}$ of dispersion; 1200 grooves mm$^{−1}$) and a Hamamatsu R13456 red sensitive Peltier-cooled PMT detector. Emission and excitation spectra were corrected for source intensity (lamp and grating) and emission spectral response (detector and grating) by standard correction curves. Time-resolved measurements were performed using either the Time-Correlated Single-Photon Counting (TCSPC) or the Multi-Channel Scaling (MCS) electronics option of the TimeHarp 260 board installed on a PicoQuant FluoTime 300

fluorimeter (PicoQuant GmbH, Germany), equipped with a PDL 820 laser pulse driver. A pulsed laser diode either LDH-P-C-375 ($\lambda = 375$ nm) or LDH-P-C-440B ($\lambda = 440$ nm) with pulse full width at half maximum <50 ps, repetition rate 200 kHz–40 MHz was used to excite the sample and mounted directly on the sample chamber at 90°. The photons were collected by a PMA Hybrid-07 single photon counting detector. The data were acquired by using the commercially available software EasyTau II (PicoQuant GmbH, Germany), while data analysis was performed using the built-in software FluoFit (PicoQuant GmbH, Germany). Luminescence quantum yields were measured in optically dilute solutions (optical density <0.1 at the excitation wavelength) and compared to reference emitter by following the method of Demas and Crosby.[31] The Ru(bpy)$_3$Cl$_2$ complex in air-equilibrated water solution at room temperature was used as reference (PLQY = 0.04).[32] For solid-state samples, the absolute photoluminescence quantum yields (PLQY) were measured on a Hamamatsu Quantaurus-QY C11347-11 integrating sphere in air-equilibrated condition using an empty quartz tube as the reference upon excitation at $\lambda_{exc} = 400$–480 nm. All the solvents were spectrophotometric grade. Dearated samples were prepared by the freeze-pump-thaw technique by using a home-made quartz cuvette equipped with a Rotaflo stopcock. Thin-film samples were prepared by spin-coating method from a CH$_2$Cl$_2$ solution of either **complex** : polymethylmetacrylate (PMMA) or **complex** : ionic liquid mixture.

For time resolved measurements, data fitting was performed by employing the maximum likelihood estimation (MLE) methods and the quality of the fit was assessed by inspection of the reduced χ^2 function and of the weighted residuals. For multi-exponential decays, the intensity, namely I(t), has been assumed to decay as the sum of individual single exponential decays (*eqn.* 2):

$$I(t) = \sum_{i=1}^{n} \alpha_i exp\left(-\frac{t}{\tau_i}\right) \qquad\qquad eqn.\ 2$$

where τ_i are the decay times and α_i are the amplitude of the component at $t = 0$. In the tables, the percentages to the pre-exponential factors, α_i, are listed upon normalization. Intensity average lifetimes were calculated by using the following equation (*eqn*. 3):[33]

$$\bar{\tau} = \frac{a_1\tau_1^2 + a_2\tau_2^2}{a_1\tau_1 + a_2\tau_2} \qquad\qquad eqn.\ 3$$

Computational details

All calculations have been performed with ADF 2019[34] at DFT level of theory (B3LYP functional).[35] All atoms were described by the DZP basis set except the copper cations which were described by the TZP basis set.[36] Scalar Hamiltonian ZORA was used.[37] Weak interactions were included through Grimme's corrections.[38] Solvent (DCM) was introduced by means of Polarized Continuum Model (PCM) formalism.[39] All structures were fully optimized and absorption spectra computed by mean of TD-DFT[40] on these optimal structures. Excited states geometries were optimized in the same conditions with a triplet wavefunction in unrestricted formalism. Spin-Orbit Coupling element were computed by perturbation of the TD-DFT calculations [41]. To avoid triplet instability Tamm-Dancoff approximation was used.[42] The nature of the excited states was determined either by mean of THEODore analysis[43] or by electron density difference between ground and excited state computed with DGrid package.[44] Both were extracted from ADF wavefunctions. Non-Covalent Interactions were computed using NCIPlot package [45] on the ADF optimized structures. The procedure used to compute the NCI (promolecular approximation) does not support copper atom, for this calculation only it was replaced by Na atoms.

Electrochemical setup

Anhydrous dichloromethane (DCM, Sigma-Aldrich, 99.9%) and tetra-n-butylammonium hexafluorophosphate (TBPF$_6$, Sigma-Aldrich, 99%) were used as received. The working electrode was a glassy-carbon disk electrode (2 mm diameter, Princeton Applied Research GO224). The electrode was polished as already described elsewhere.[46] Before experiments, the electrode was further polished with a 0.05 μm polycrystalline diamond suspension (Buehler, MetaDI) and electrochemically activated in the background solution by means of several voltammetric cycles at 0.5 V s^{-1} between the anodic and the cathodic solvent/electrolyte discharges, until the expected quality features were attained.[47] A platinum wire served as the counter electrode and a silver wire, separated from the main electrolytic compartment by a Vycor® frit, was used as a quasi-reference electrode. At the end of each experiment, its potential was calibrated against the ferricenium/ferrocene couple (Fc), used as an internal redox standard. Therefore, all the potentials against Fc. The cyclic voltammetry (CV) and differential pulse voltammetry (DPV) experiments were carried out in DCM/0.1 M TBPF$_6$ under an Ar atmosphere, using a 1 mM concentration for the electroactive compound. An SP300 Electrochemical Workstation (BioLogic) was used. For the CV experiments, we employed the feedback correction to minimize the ohmic drop between the working and the reference

electrodes. For the DPV experiments we employed a pulse width of 100 ms, a pulse heigh of 5 mV and a step of 500 ms in between two consecutive pulses.

LEC device fabrication and characterization

For device fabrication, standard clean and UV/ozone treatment were performed on the indium-tin oxide (ITO) coated glass substrates. After cleaning, the substrates were spin-coated with a poly(3,4-ethylenedioxythiophene):poly(styrene sulfonate) (PEDOT:PSS) layer (40 nm) at 3500 rpm and was then baked at 150 °C for 30 min in ambient air. The mixture of complex (either **Cu-NIR1** or **Cu-NIR2**) (80 wt.%) and 1-butyl-3-methylimidazolium hexafluorophosphate [BMIM$^+$(PF$_6$$^-$)] (20 wt.%) in acetonitrile solution was spun on top of the PEDOT:PSS layer. The ionic liquid [BMIM$^+$(PF$_6$)$^-$] was added to provide additional mobile ions to accelerate device response. Various solution concentrations (40, 60, and 80 mg mL^{-1}) were utilized in spin coating to deposit different emissive-layer thicknesses for device performance optimization. To improve the device performance, the yellow complex **YIr** (Figure S51), which exhibits superior carrier balance,[23] was incorporated in the emissive layer of complex **Cu-NIR1** or **Cu-NIR2**. The weight ratios of the mixed solution of complex **Cu-NIR1** or **Cu-NIR2**, complex **YIr**, and [BMIM$^+$(PF$_6$)$^-$] were (80-x), x, and 20 wt.%, respectively (x = 8, 12, 16, or 20). The solution concentration for spin coating of the **YIr** doped emissive layer was 60 mg mL^{-1}. In addition, complex **Cu-NIR1** was doped in the blue-green complex **B** (Figure S51) to generate white EL emission. The weight ratios of the mixed solution of complex **B**, complex **Cu-NIR1**, and [BMIM$^+$(PF$_6$)$^-$] were 79.4, 0.6, and 20 wt.%, respectively. The solution concentration for spin coating of the white emissive layer was 60 mg mL^{-1}. Spin coating of all emissive layers was performed at 2000 rpm in ambient air. The thicknesses of the emissive layers were measured by ellipsometry (*cf.* Table 3 and S15). After depositing the emissive layers, the samples were baked at 60 °C for 8 hours in a vacuum oven to remove the residual solvent. Finally, a silver top contact was deposited by thermal evaporation in a vacuum chamber (*ca.* 10^{-6} torr). The EL emission properties of these LECs were measured using source-measurement units (B2901A, Keysight) and a calibrated Si photodiode. The EL spectra of these LECs were acquired with a calibrated fiber-optic spectrometer (USB2000+, Ocean Optics). All LEC devices were measured under constant bias voltages except the white LECs, which were tested under constant currents. Device measurements were performed in a nitrogen glove box to reduce the device degradation rate.
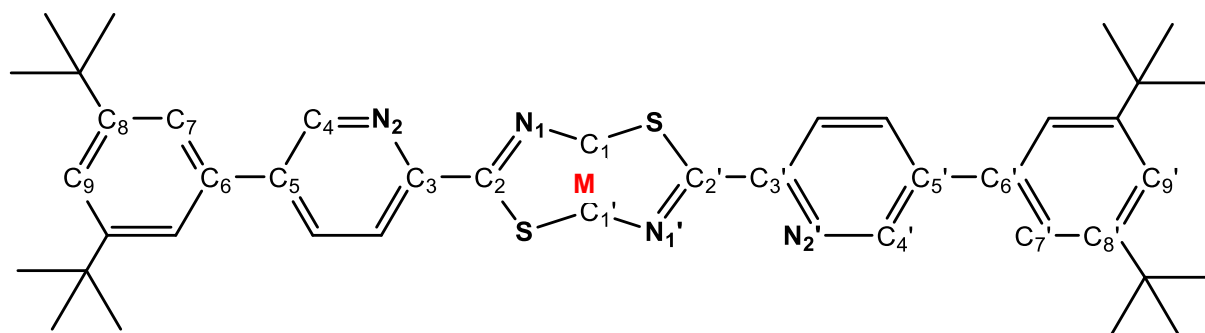
Supplementary Schemes
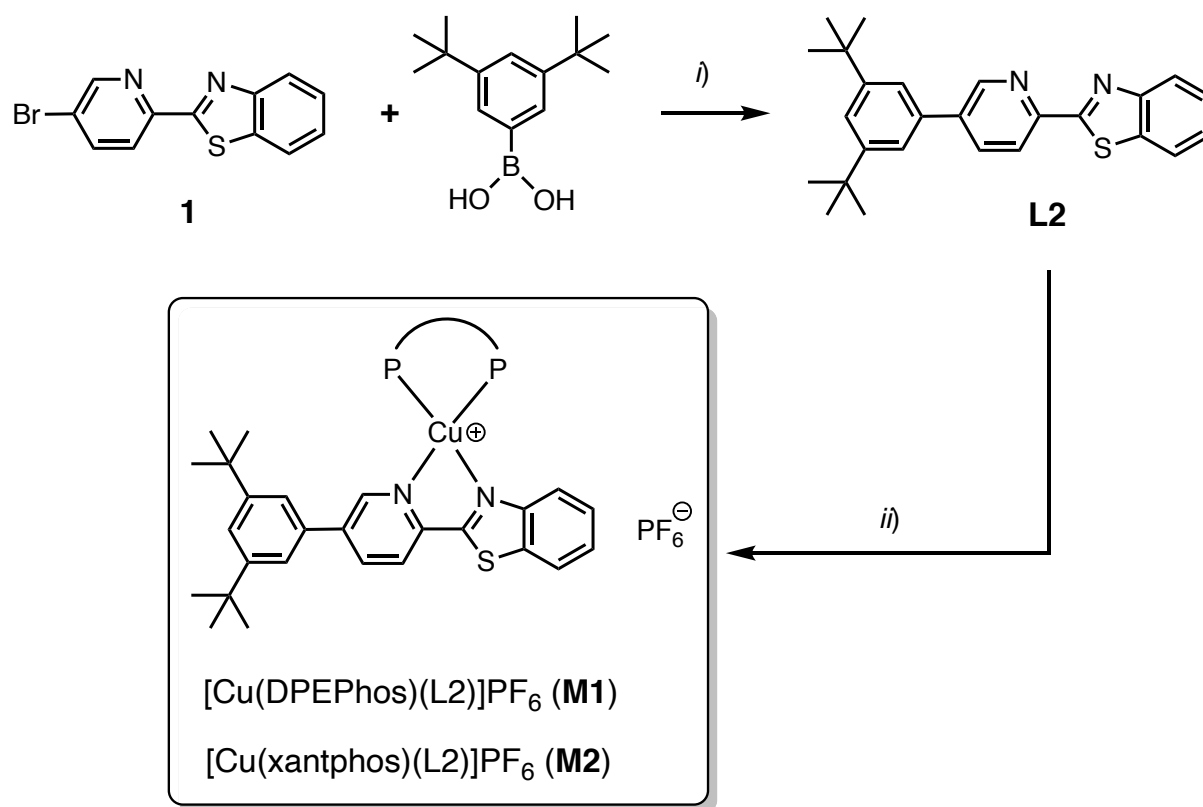
Scheme S1. Synthetic pathway employed for the synthesis of mononuclear compound **M1** and **M2**. Conditions: *i*) Na$_2$CO$_3$, Pd(Ph$_3$)$_4$, 1,4-dioxane/H$_2$O, reflux; *ii*) Cu(CH$_3$CN)$_4$PF$_6$, CH$_2$Cl$_2$, room temperature, diphosphine (either DPEPhos or Xantphos).
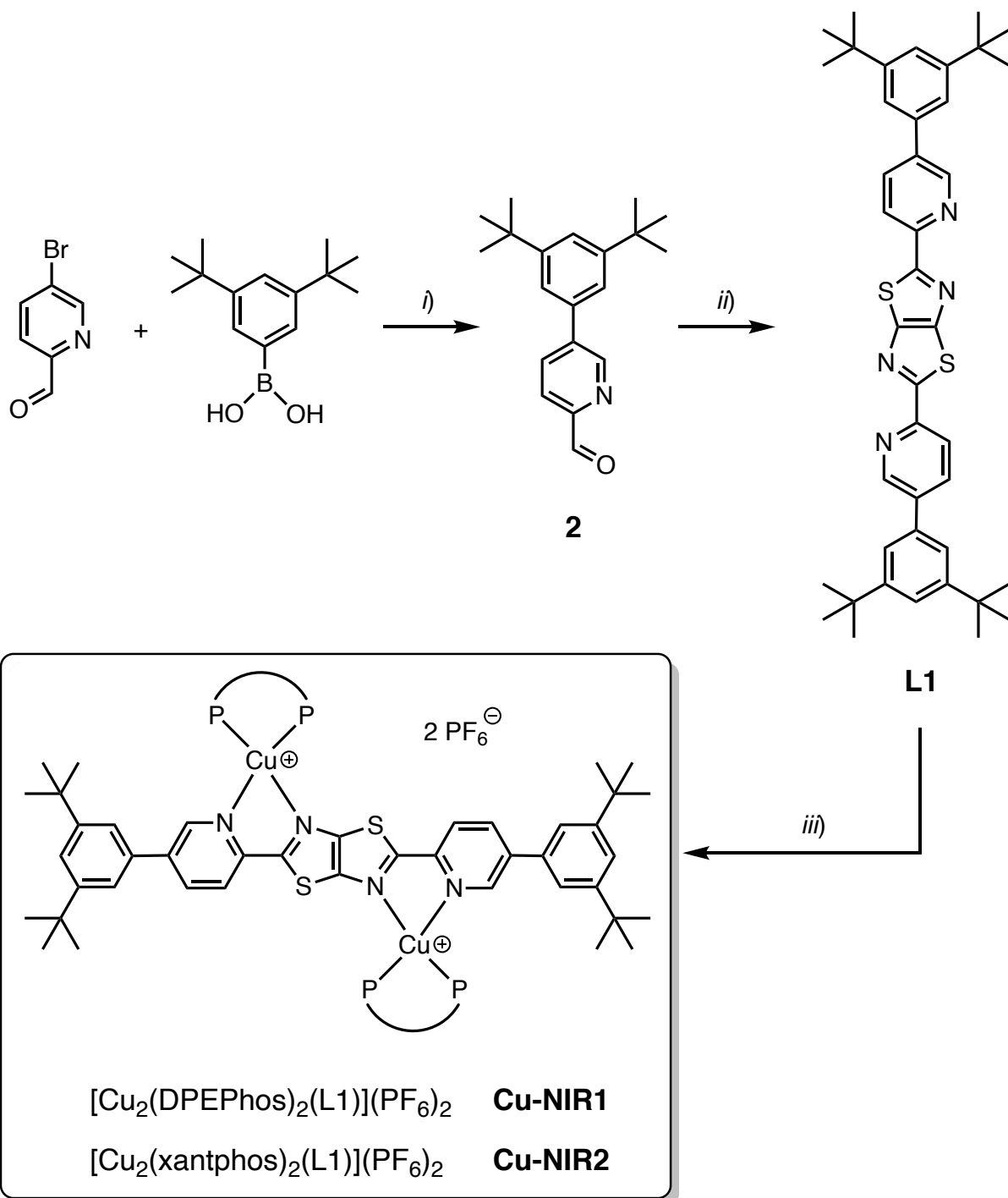
Scheme S2. Synthetic pathway employed for the synthesis of dinuclear compound **Cu-NIR1** and **Cu-NIR2**. Conditions: *i*) K$_2$CO$_3$, Pd(Ph$_3$)$_4$, DMF, 90ºC; *ii*) dithiooxamide, DMF, reflux; *iii*) Cu(CH$_3$CN)$_4$PF$_6$, CH$_2$Cl$_2$, room temperature, diphosphine (either DPEPhos or Xantphos).

Scheme S3. Atom labeling used for pro-ligand **L1**. M is center of the C_1–C_1' bond.
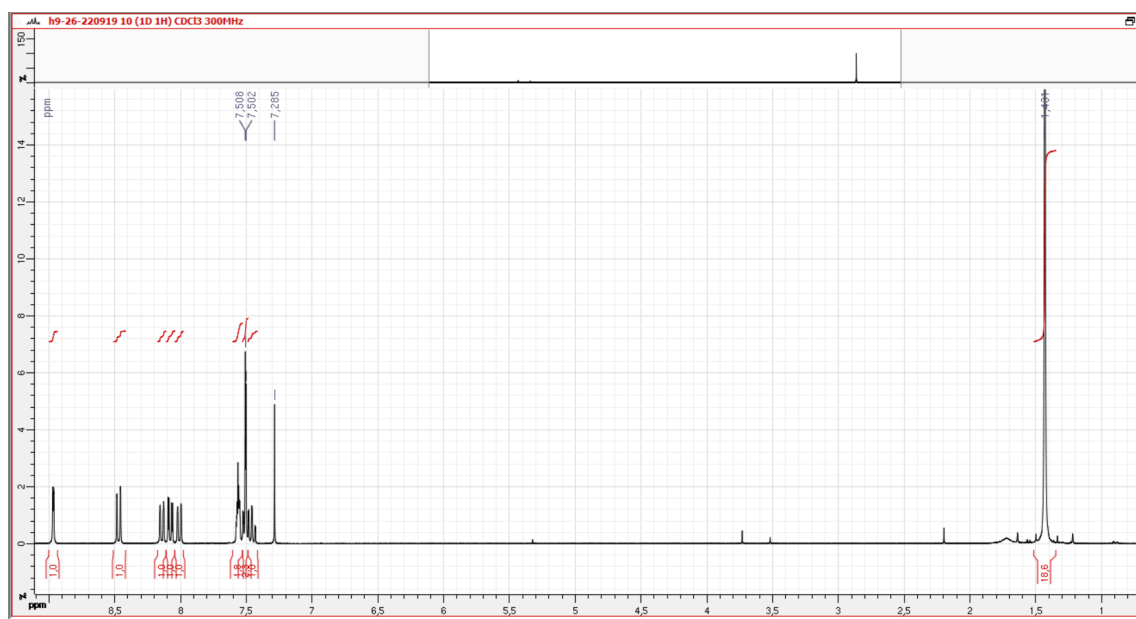
Supplementary Figures

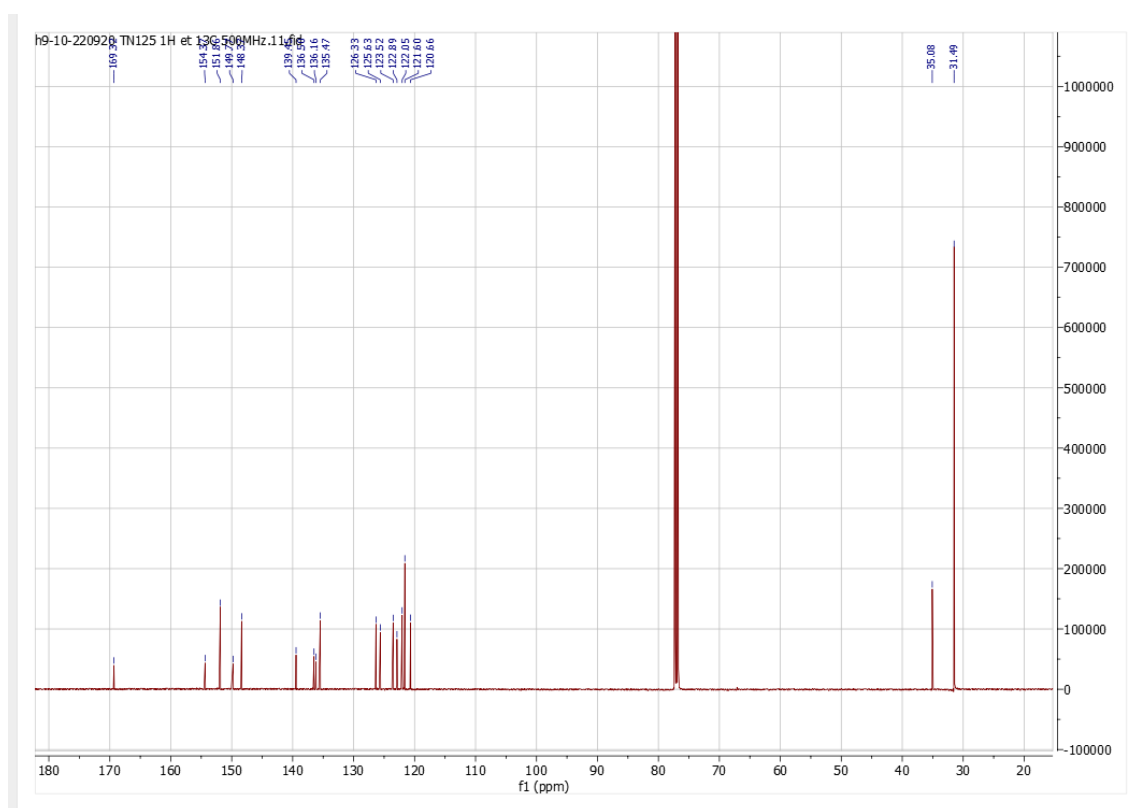**Figure S1.** ^{1}H NMR (500 MHz, CDCl$_3$, 298 K) spectrum recorded for compound **L2**.

Figure S2. ^{13}C{^{1}H} NMR (125 MHz, CDCl$_3$, 298 K) spectrum recorded for compound **L2**.

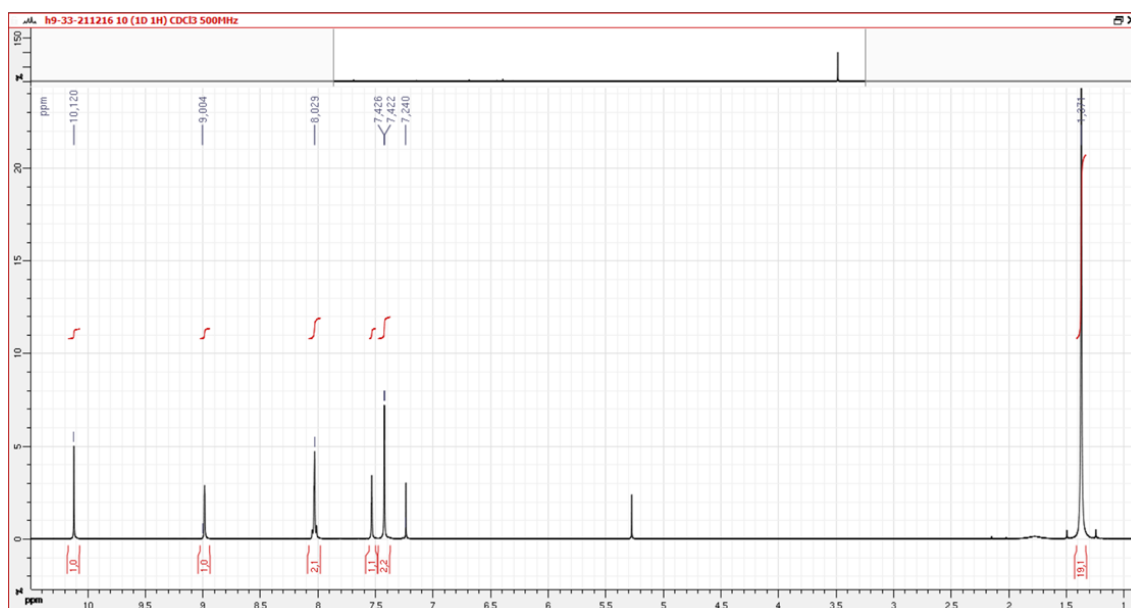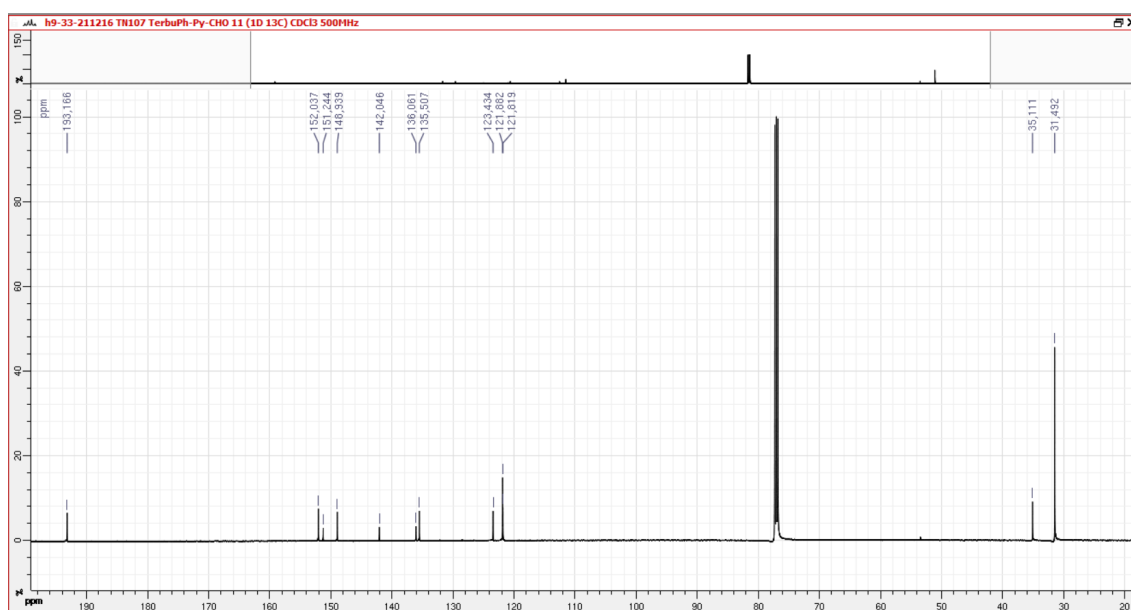**Figure S3.** ^{1}H NMR (500 MHz, CDCl$_3$, 298 K) recorded for compound **2**.

Figure S4. ^{13}C{^{1}H} NMR (125 MHz, CDCl$_3$, 298 K) spectrum recorded for compound **2**.

Figure S5. ^{1}H NMR (500 MHz, CDCl$_3$, 298 K) spectrum recorded for compound **L1**.

Figure S6. ^{13}C{^{1}H} NMR (125 MHz, CDCl$_3$, 298 K) spectrum recorded for compound **L1**.

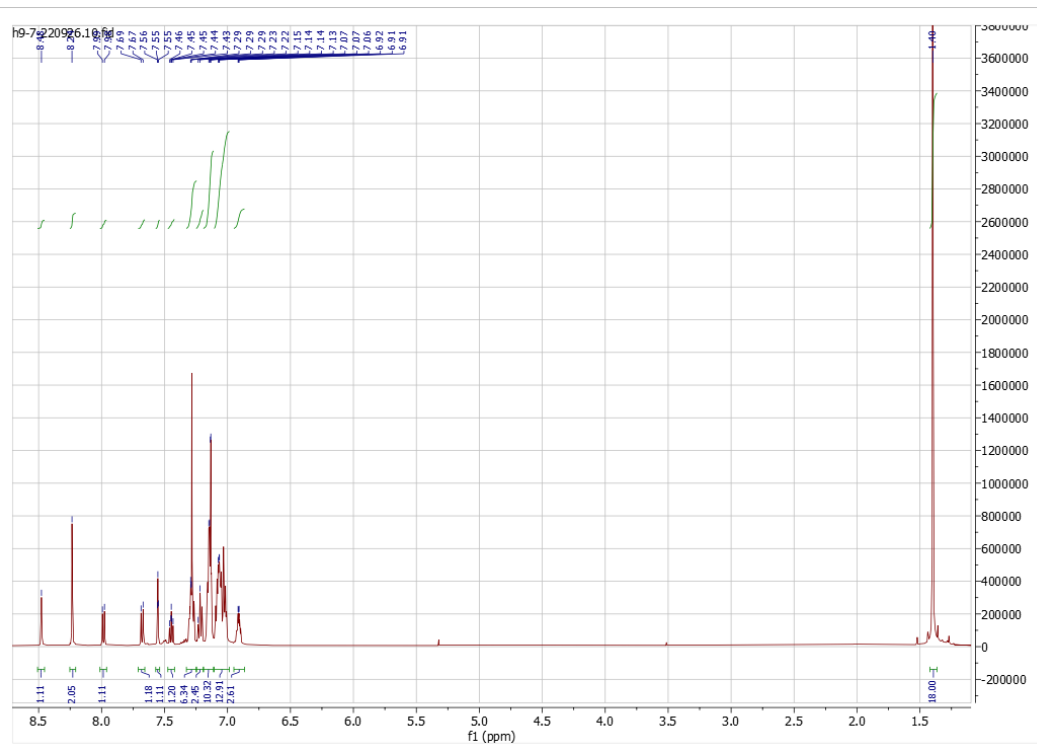**Figure S7.** ^{1}H NMR (500 MHz, CDCl$_3$, 298 K) spectrum recorded for compound **M1**.

Figure S8. ^{13}C{^{1}H} NMR (125 MHz, CDCl$_3$, 298 K) spectrum recorded for compound **M1**.

Figure S9. ^{1}H NMR (500 MHz, CDCl$_3$, 298 K) spectrum recorded for compound **M2**.

Figure S10. $^{13}C\{^{1}H\}$ NMR (125 MHz, CDCl$_3$, 298 K) spectrum recorded for compound **M2**.

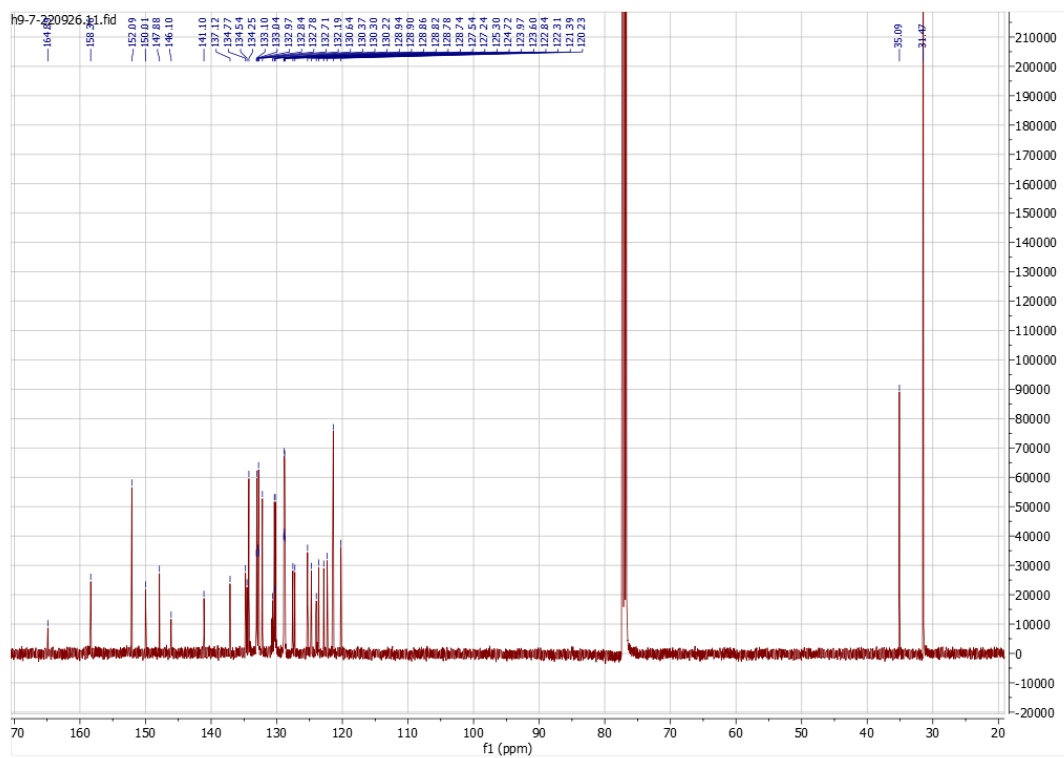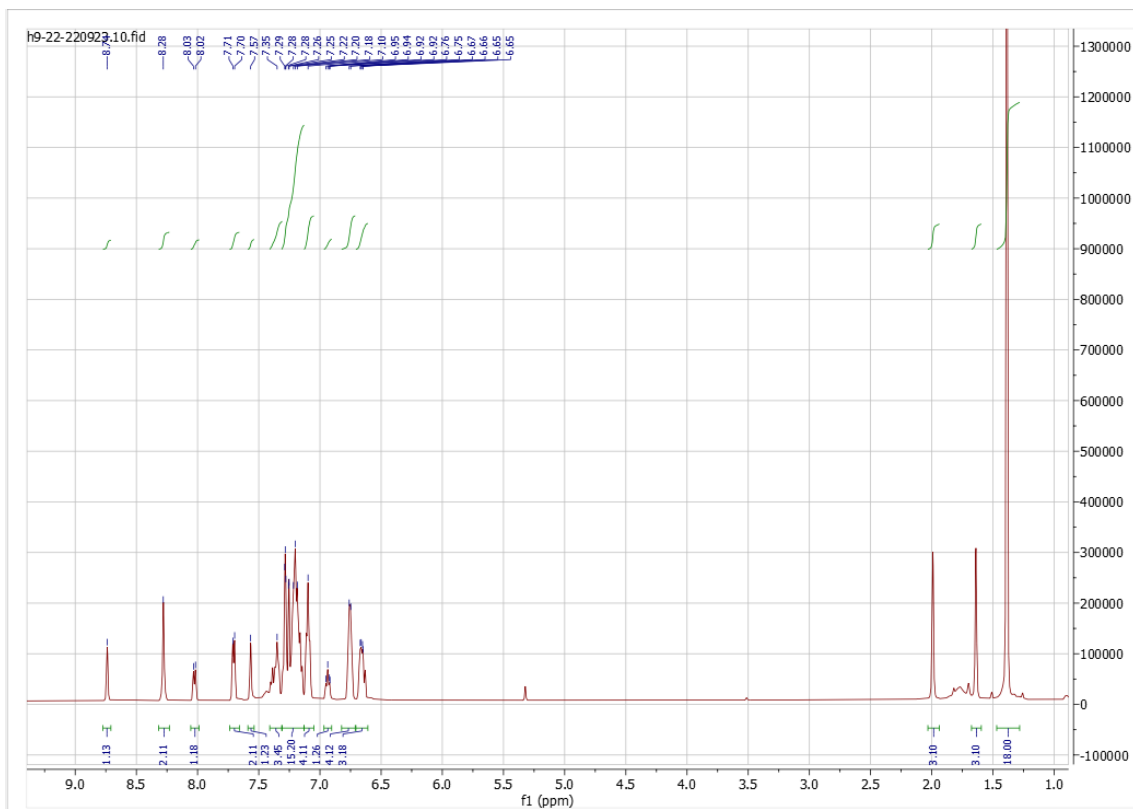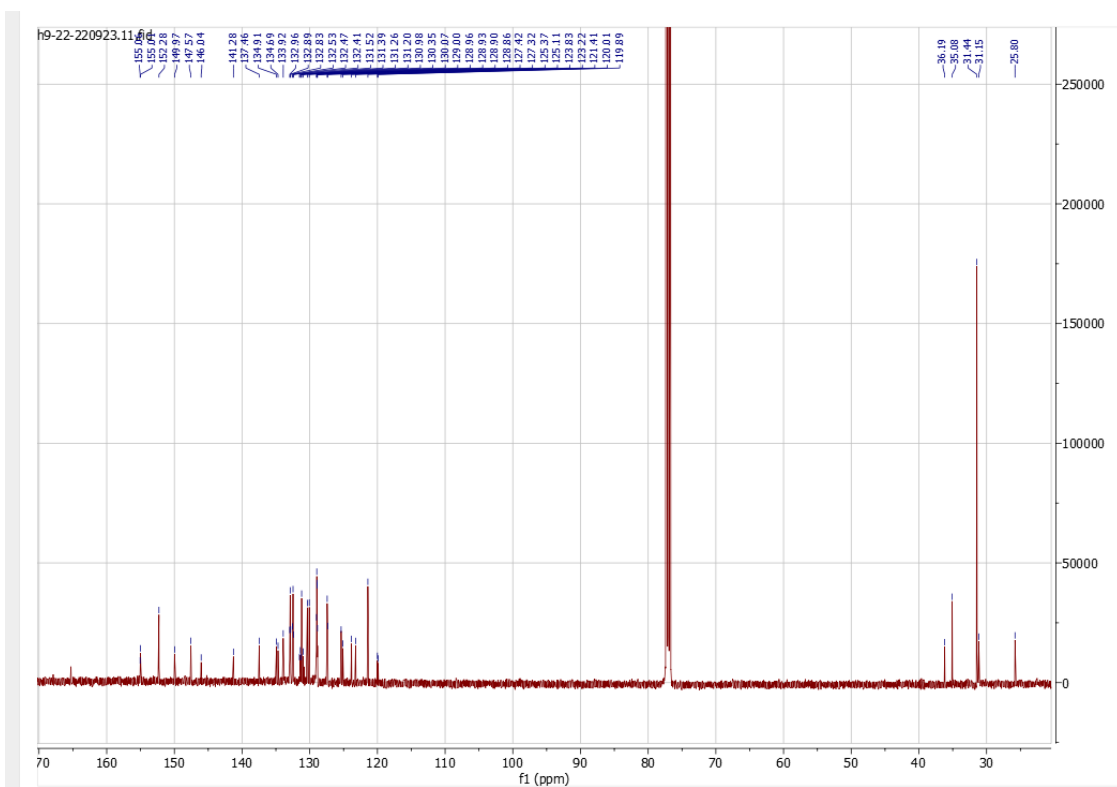**Figure S11.** ^{1}H NMR (500 MHz, CDCl$_3$, 298 K) spectrum recorded for compound **Cu-NIR1**.

Figure S12. ^{13}C{^{1}H} NMR (125 MHz, CDCl$_3$, 298 K) spectrum recorded for compound **Cu-NIR1**.

Figure S13. ^{1}H NMR (500 MHz, CDCl$_3$, 298 K) spectrum recorded for compound **Cu-NIR2**.

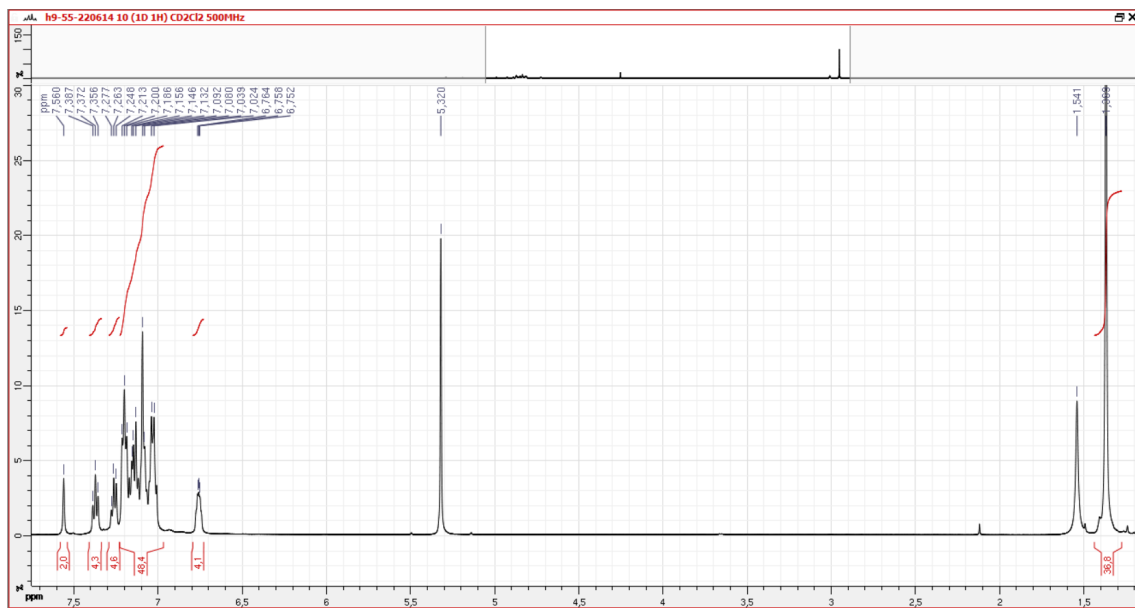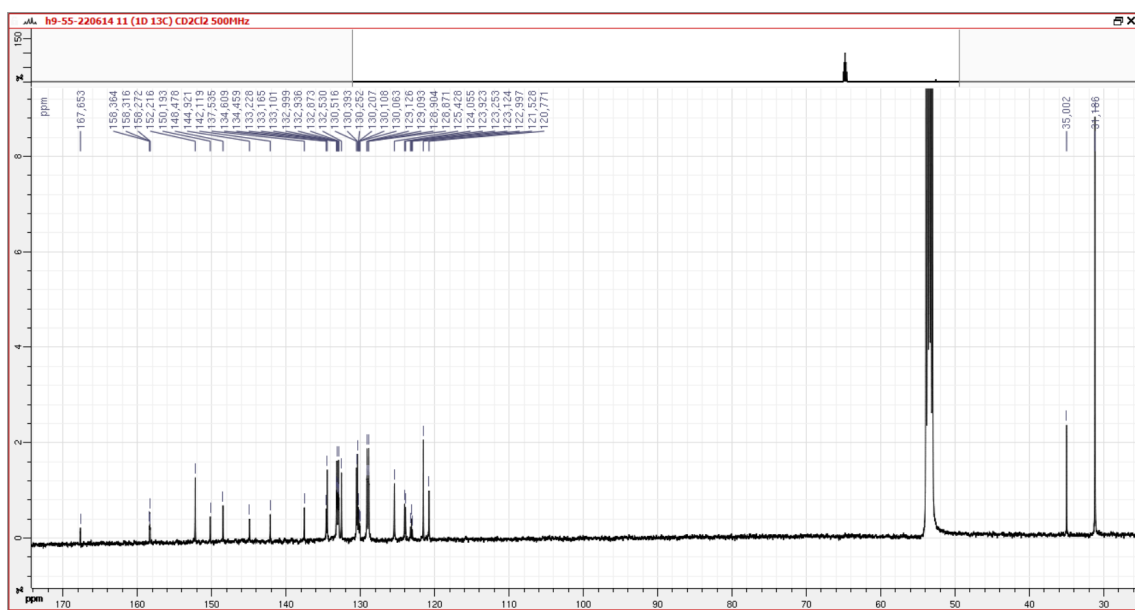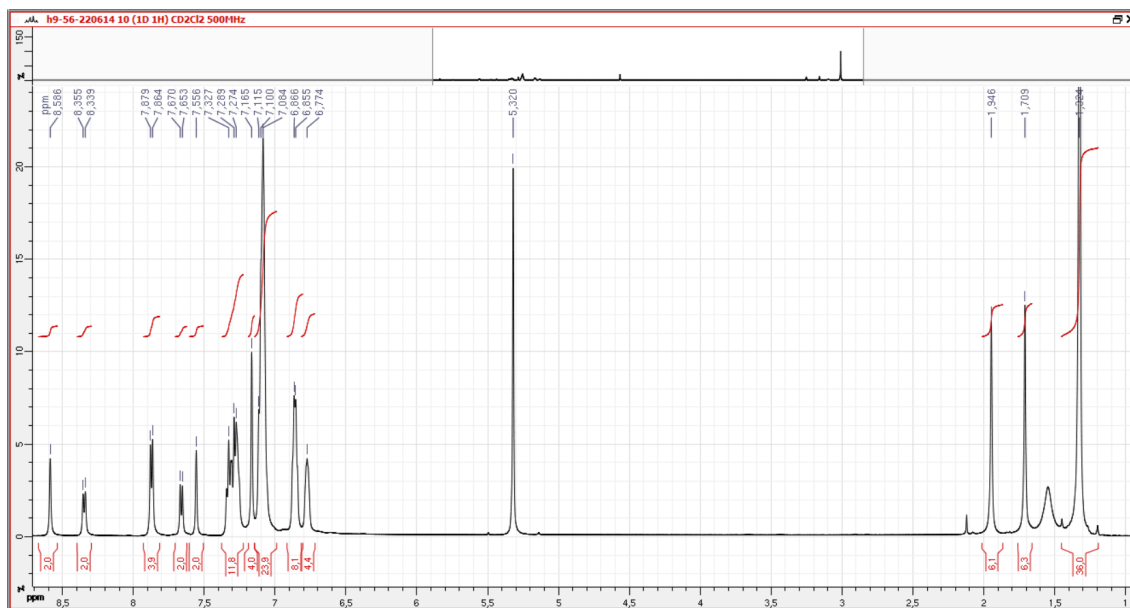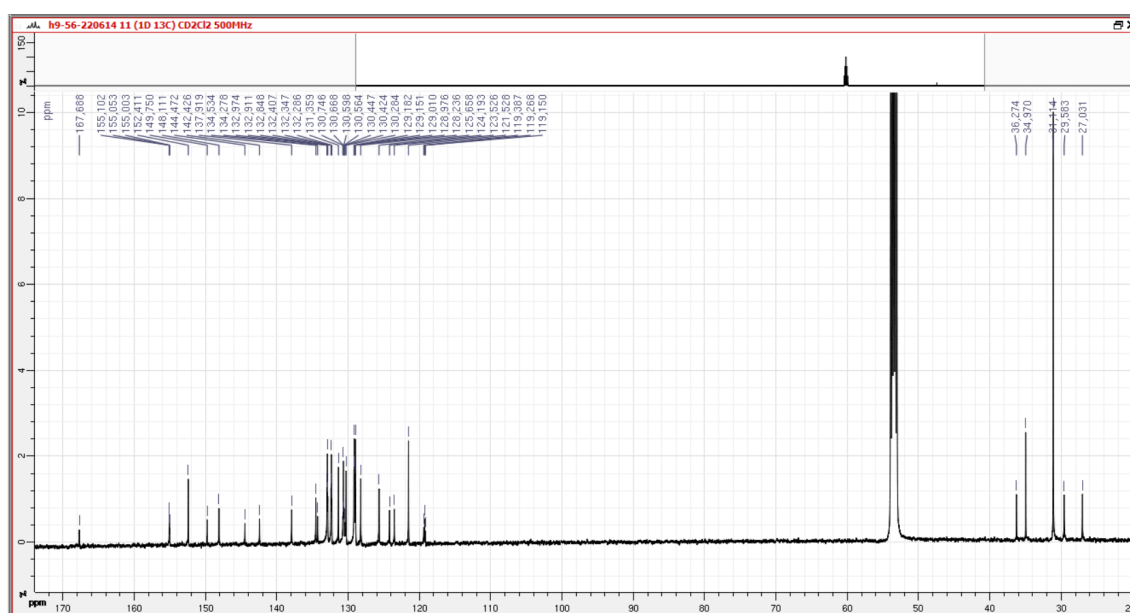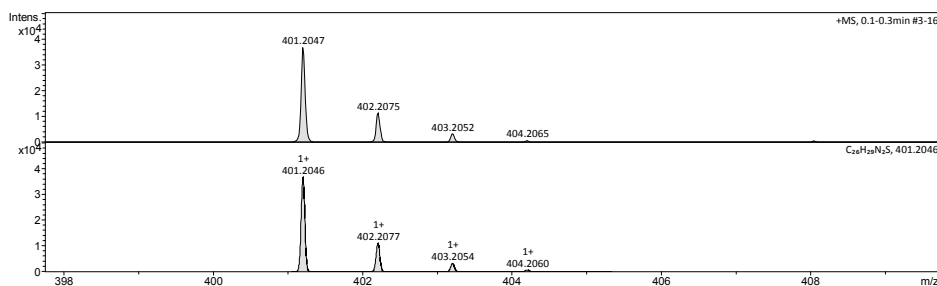**Figure S14.** ^{13}C{^{1}H} NMR (125 MHz, CDCl$_3$, 298 K) spectrum recorded for compound **Cu-NIR2**.

Figure S15. HR-ESI-MS spectrum of compound **L2**.

Figure S16. HR-ESI-MS spectrum of compound **2**.

Mass Spectrum HR Report

Analysis Info
Analysis Name: D:\Data\SMasse\2022\09_Septembre 2022\F13299SK.d
Method: Tune_pos_Mid.m
Sample Name: TN108
Comment

Acquisition Date: 9/21/2022 3:19:34 PM
Operator: BDAL@DE
Instrument: micrOTOF II 8213750.1045 1

Acquisition Parameter

Source Type	ESI	Ion Polarity	Positive	Set Corrector Fill	49.7 V
n/a	n/a	n/a	n/a	n/a	n/a
Scan Begin	50 m/z	n/a	n/a	Set Reflector	1800.0 V
Scan End	3000 m/z	n/a	n/a	Set Flight Tube	8600.0 V
		n/a	n/a	Set Detector TOF	2020.0 V

+MS, 0.5-1.0min #29-60
C₄₂H₄₉N₄S₂, 673.3393

Meas. m/z	#	Ion Formula	m/z	err [ppm]	Mean err [ppm]	rdb	N-Rule	e⁻ Conf	mSigma	Std I	Std Mean m/z	Std I VarNorm	Std m/z Diff	Std Comb Dev
673.339614	1	C42H49N4S2	673.339316	-0.4	-0.7	20.5	ok	even	5.7	9.3	n.a.	n.a.	n.a.	n.a.

Figure S17. HR-ESI-MS spectrum of compound **L1**.

Mass Spectrum HR Report

Analysis Info
Analysis Name: Y:\2022\09_Septembre 2022\F13347SK.d
Method: Tune_pos_Mid.m
Sample Name: TN126
Comment

Acquisition Date: 26/09/2022 14:37:06
Operator: BDAL@DE
Instrument: micrOTOF II 8213750.10451

Acquisition Parameter

Source Type	ESI	Ion Polarity	Positive	Set Corrector Fill	49.7 V
n/a	n/a	n/a	n/a	n/a	n/a
Scan Begin	50 m/z	n/a	n/a	Set Reflector	1800.0 V
Scan End	3000 m/z	n/a	n/a	Set Flight Tube	8600.0 V
		n/a	n/a	Set Detector TOF	2020.0 V

+MS, 0.1-0.2min #4-11
C₆₂H₅₆CuN₂OP₂S, 1001.2879

Meas. m/z	#	Ion Formula	m/z	err [ppm]	Mean err [ppm]	rdb	N-Rule	e⁻ Conf	mSigma	Std I	Std Mean m/z	Std I VarNorm	Std m/z Diff	Std Comb Dev
1001.287345	1	C62H56CuN2OP2S	1001.287908	0.6	1.0	36.5	ok	even	4.9	4.1	n.a.	n.a.	n.a.	n.a.

Figure S18. HR-ESI-MS spectrum of compound **M1**.

Mass Spectrum HR Report

Analysis Info

				Acquisition Date	26/09/2022 14:49:52
Analysis Name	Y:\2022\09_Septembre 2022\F13348SK.d				
Method	Tune_pos_Mid.m			Operator	BDAL@DE
Sample Name	TN126			Instrument	micrOTOF II 8213750.10451
Comment					

Acquisition Parameter

					Set Corrector Fill	49.7 V
Source Type	ESI	Ion Polarity	Positive		n/a	n/a
n/a	n/a	n/a	n/a		n/a	n/a
Scan Begin	50 m/z	n/a	n/a		Set Reflector	1800.0 V
Scan End	3000 m/z	n/a	n/a		Set Flight Tube	8600.0 V
		n/a	n/a		Set Detector TOF	2020.0 V

Intens. x10^5 — +MS, 0.1-0.3min #3-20

1041.3204, 1042.3239, 1043.3212, 1044.3228, 1045.3244, 1046.3242

$C_{65}H_{60}CuN_2OP_2S$, 1041.3192

1+ 1041.3192, 1+ 1042.3225, 1+ 1043.3202, 1+ 1044.3217, 1+ 1045.3229, 1+ 1046.3240

Meas. m/z	#	Ion Formula	m/z	err [ppm]	Mean err [ppm]	rdb	N-Rule	e⁻	Conf	mSigma	Std I	Std Mean m/z	Std I VarNorm	Std m/z Diff	Std Comb Dev
1041.320359	1	C65H60CuN2OP2S	1041.319208	-1.1	-1.1	37.5	ok	even		10.3	6.3	n.a.	n.a.	n.a.	n.a.

Bruker Compass DataAnalysis 4.2   printed: 27/09/2022   10:33:34   Page 1 of 1
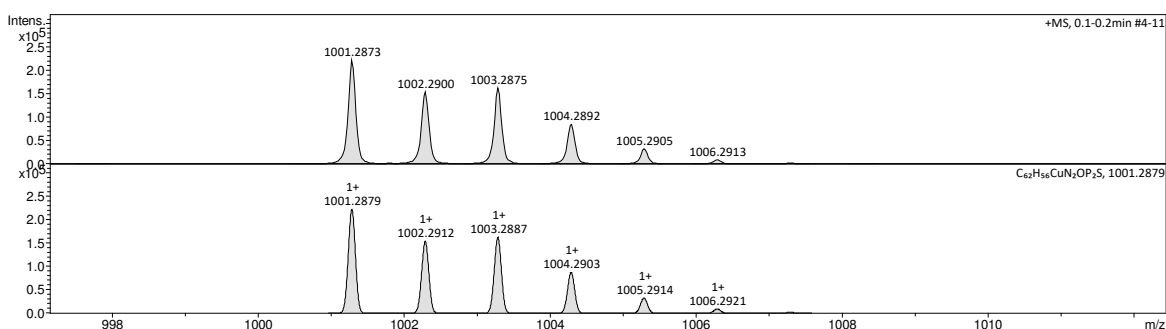
Figure S19. HR-ESI-MS spectrum of compound **M1**.

Mass Spectrum HR Report

Analysis Info

				Acquisition Date	26/09/2022 15:01:21
Analysis Name	Y:\2022\09_Septembre 2022\F13349SK.d				
Method	Tune_pos_Mid.m			Operator	BDAL@DE
Sample Name	TN111			Instrument	micrOTOF II 8213750.10451
Comment					

Acquisition Parameter

					Set Corrector Fill	49.7 V
Source Type	ESI	Ion Polarity	Positive		n/a	n/a
n/a	n/a	n/a	n/a		n/a	n/a
Scan Begin	50 m/z	n/a	n/a		Set Reflector	1800.0 V
Scan End	3000 m/z	n/a	n/a		Set Flight Tube	8600.0 V
		n/a	n/a		Set Detector TOF	2020.0 V

Intens. — +MS, 0.0-1.0min #1-50

2019.4734, 2020.4791, 2021.4796, 2022.4785, 2023.4779, 2024.4785, 2025.4847, 2026.4893, 2027.4783, 2028.5293

$C_{114}H_{104}Cu_2F_6N_4O_2P_5S_2$, 2019.4779

1+ 2019.4779, 1+ 2020.4812, 1+ 2021.4798, 1+ 2022.4810, 1+ 2023.4811, 1+ 2024.4816, 1+ 2025.4824, 1+ 2026.4832, 1+ 2027.4843

Meas. m/z	#	Ion Formula	m/z	err [ppm]	Mean err [ppm]	rdb	N-Rule	e⁻	Conf	mSigma	Std I	Std Mean m/z	Std I VarNorm	Std m/z Diff	Std Comb Dev
2019.473449	1	C114H104Cu2F6N4O2P5S2	2019.477944	2.2	0.8	63.5	ok	even		17.6	10.0	n.a.	n.a.	n.a.	n.a.

Bruker Compass DataAnalysis 4.2   printed: 27/09/2022   10:41:54   Page 1 of 1

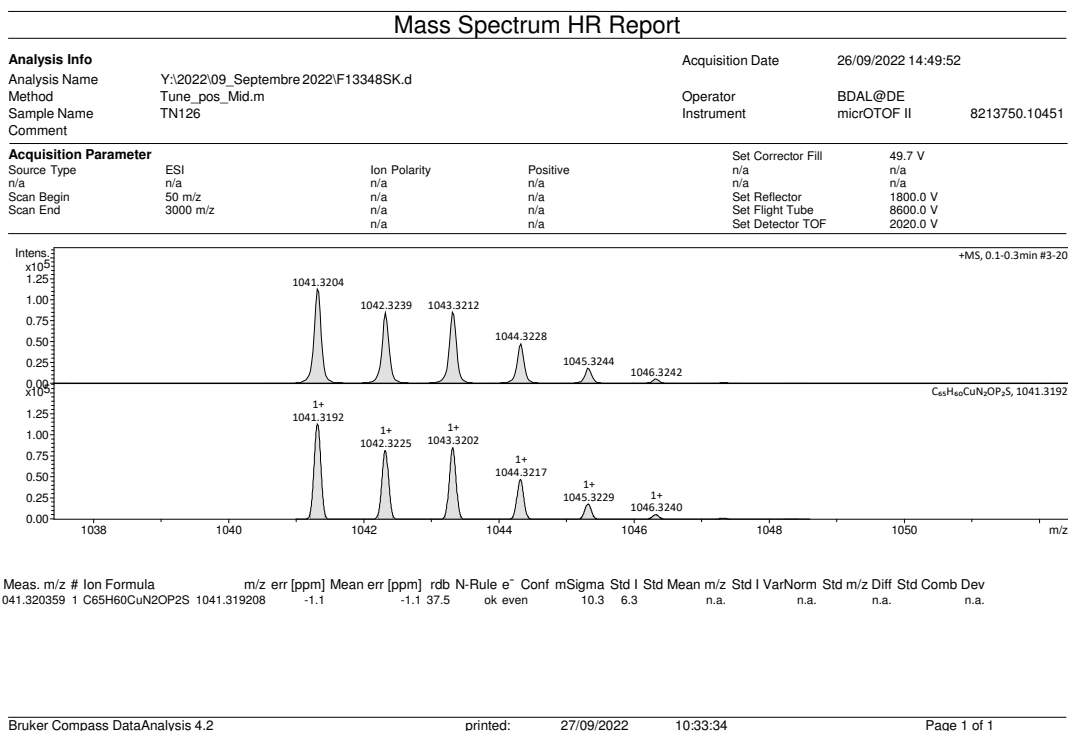**Figure S20.** HR-ESI-MS spectrum of compound **Cu-NIR1**.

Analysis Info

				Acquisition Date	12/07/2022 14:23:12
Analysis Name	Y:\2022\07_Juillet 2022\F12840SK.d				
Method	Tune_pos_Mid.m			Operator	BDAL@DE
Sample Name	TN110			Instrument	micrOTOF II	8213750.10451
Comment	CH2Cl2				

Acquisition Parameter

						Set Corrector Fill	49.7 V
Source Type	ESI		Ion Polarity		Positive	n/a	n/a
n/a	n/a		n/a		n/a	n/a	n/a
Scan Begin	50 m/z		n/a		n/a	Set Reflector	1800.0 V
Scan End	3000 m/z		n/a		n/a	Set Flight Tube	8600.0 V
			n/a		n/a	Set Detector TOF	2020.0 V

Meas. m/z # Ion Formula	m/z err [ppm]	Mean err [ppm]	rdb	N-Rule	e⁻	Conf	mSigma	Std I	Std Mean m/z	Std I	VarNorm	Std m/z Diff	Std Comb Dev
2099.537965 1 C120H112Cu2F6N4O2P5S2 2099.540545	1.2	480.4	65.5	ok	even		33.3	23.9	n.a.	n.a.		n.a.	n.a.

Bruker Compass DataAnalysis 4.2   printed: 13/07/2022   14:16:05   Page 1 of 1

Figure S21. HR-ESI-MS spectrum of compound **Cu-NIR2**.
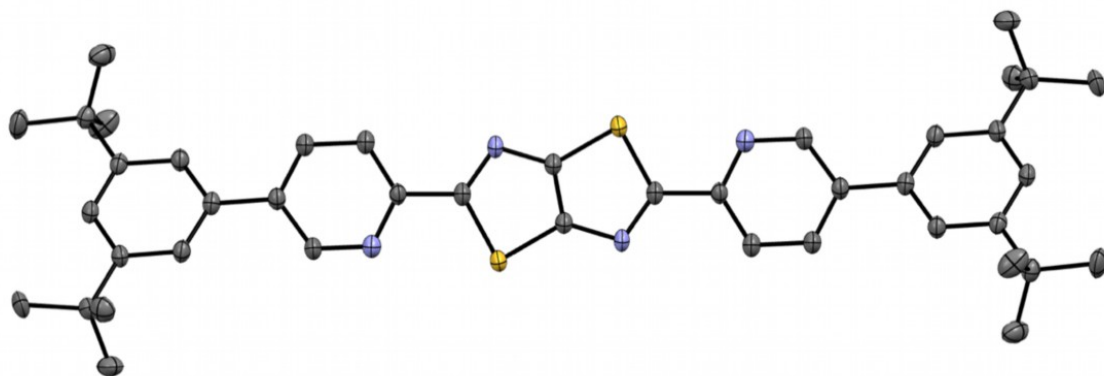
Figure S22. ORTEP diagram of compound **L1** with thermal ellipsoids shown at 50% probability level obtained by single-crystal X-ray diffractometric analysis. Hydrogen atoms are omitted for clarity.
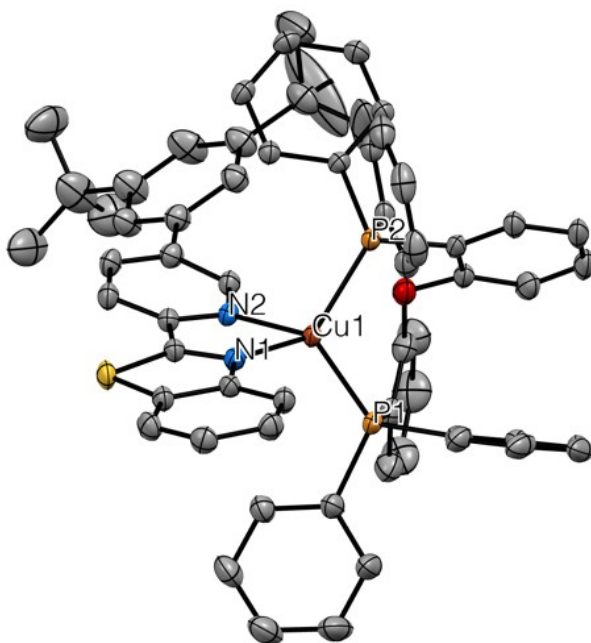

Figure S23. ORTEP diagram of compound **M1** with thermal ellipsoids shown at 50% probability level obtained by single-crystal X-ray diffractometric analysis. Hydrogen atoms and solvent molecules are omitted for clarity. Selected bond lengths (Å): Cu–N(1) = 2.053(3), Cu–N(2) = 2.098(3), Cu–P(1) = 2.2466(9), Cu–P(2) = 2.2469(9). Selected bond angles (°): N(1)–Ir–N(2) = 79.88(11), P(1)–Ir–P(2) = 115.18(3).
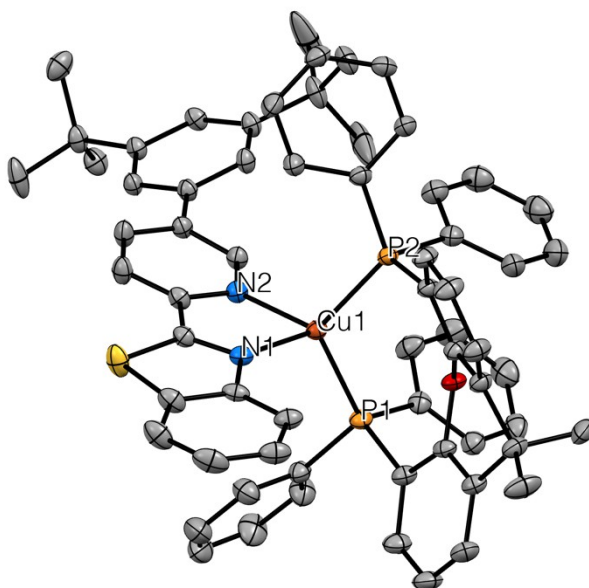
Figure S24. ORTEP diagram of compound **M2** with thermal ellipsoids shown at 50% probability level obtained by single-crystal X-ray diffractometric analysis. Hydrogen atoms are omitted for clarity. Selected bond lengths (Å): Cu–N(1) = 2.0584(17), Cu–N(2) = 2.0902(17), Cu–P(1) = 2.2629(6), Cu–P(2) = 2.2522(6). Selected bond angles (°): N(1)–Ir–N(2) = 79.46(7), P(1)–Ir–P(2) = 116.06(2).
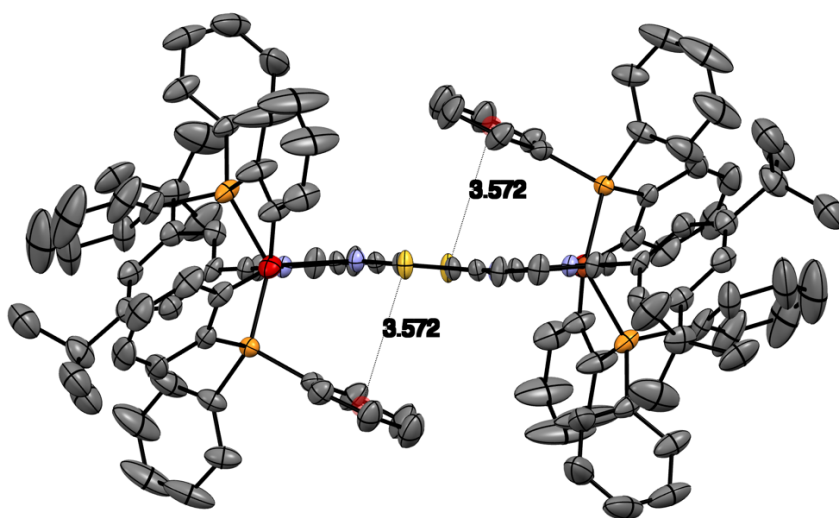

Figure S25. ORTEP diagram of compound **Cu-NIR1** with thermal ellipsoids shown at 50% probability level obtained by single-crystal X-ray diffractometric analysis. Hydrogen atoms, PF_6^- anions and solvent molecules are omitted for clarity. Selected bond lengths (Å): Cu–N(1) = 2.067(3), Cu–N(2) = 2.100(3), Cu–P(1) = 2.2444(10), Cu–P(2) = 2.2319(10). Selected bond angles (°): N(1)–Ir–N(2) = 79.67(11), P(1)–Ir–P(2) = 114.41(4).

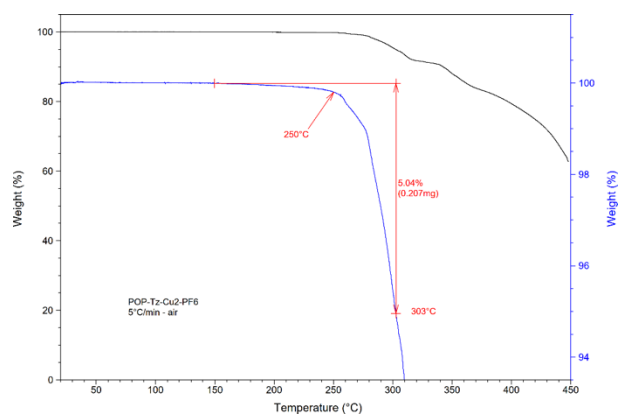**Figure S26.** Thermogravimetric analysis (TGA) curve recorded for compound **Cu-NIR1** at heating rate of 5°C min^{-1} under air.

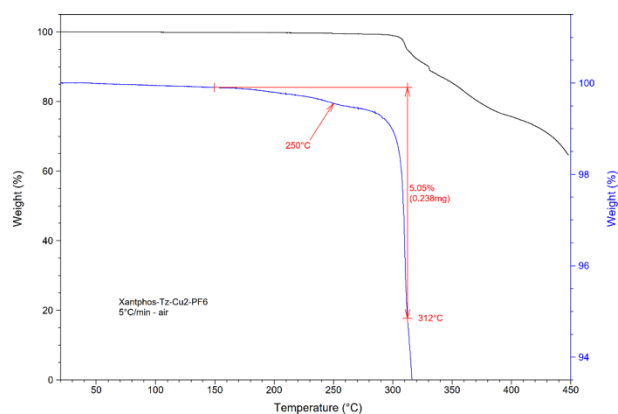**Figure S27.** Thermogravimetric analysis (TGA) curve recorded for compound **Cu-NIR2** at heating rate of 5°C min^{-1} under air.

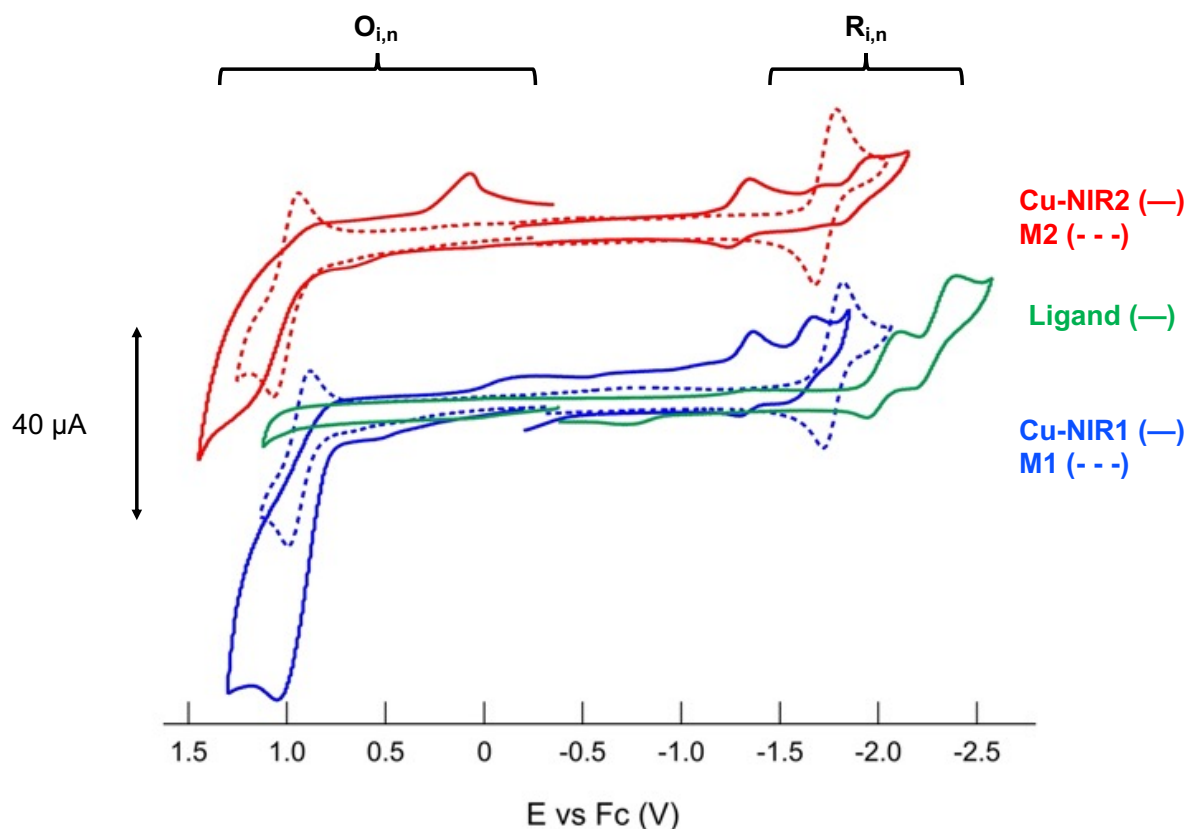**Supplementary electrochemical characterization**

Figure S28. Comparison of the CV of binuclear copper complexes Cu-NIR1 (blue curve), Cu-NIR2 (red curve) and related mononuclear counterparts M1 (blue dashed curve) and M2 (red dashed curve), and ligand (green curve) at concentration of 1 mM. The measurements were carried out in CH_2Cl_2/0.1 M $TBPF_6$. Scan rate 0.2 V s^{-1}.

Supplementary discussion #1: Electrochemical characterization.

We compared the CVs (Figure S28) and DPVs (Figure S29) of the binuclear metal complexes Cu-NIR1 and Cu-NIR2 with that of ferrocene to better understand whether the oxidation and reduction processes, $O_{1,n}$ and $R_{1,n}$ respectively, involved the exchange of one or more electrons. A few considerations deserved to be discussed:

a) Despite the concentrations of all compounds, including Fc, were 1 mM, the current intensities of the CVs of Cu-NIR1 and Cu-NIR2 appeared to be lower by a factor of 2. This is in line with the square root of the ratio of the diffusion coefficients of Fc (1.13 cm^2 s^{-1} in DMF/0.1 M TBAP)[47] and Cu-NIR1-2, which we estimated to be ~ 3 10^{-6} cm^2 s^{-1} by the CV of the $R_{1,n}$ process knowing the area of the electrode.[16]

b) The oxidation processes $O_{1,n}$ are irreversible and the experimental conditions are not ideal, due to the high ohmic drop that causes a distortion in the peak-to-peak separation (> 80 mV) also for the $Fc^0|Fc^{+1}$, thus affecting the evaluation of E_p-$E_{p/2}$ as well. Therefore, only an estimation can be made.

However, by taking into account the previous considerations and by comparing the current intensities of the $R_{1,n}$ and $O_{1,n}$ processes with the oxidation of Fc, we can confidently

state that the reduction processes are monoelectronic, whereas the oxidations might involve more than one electron.
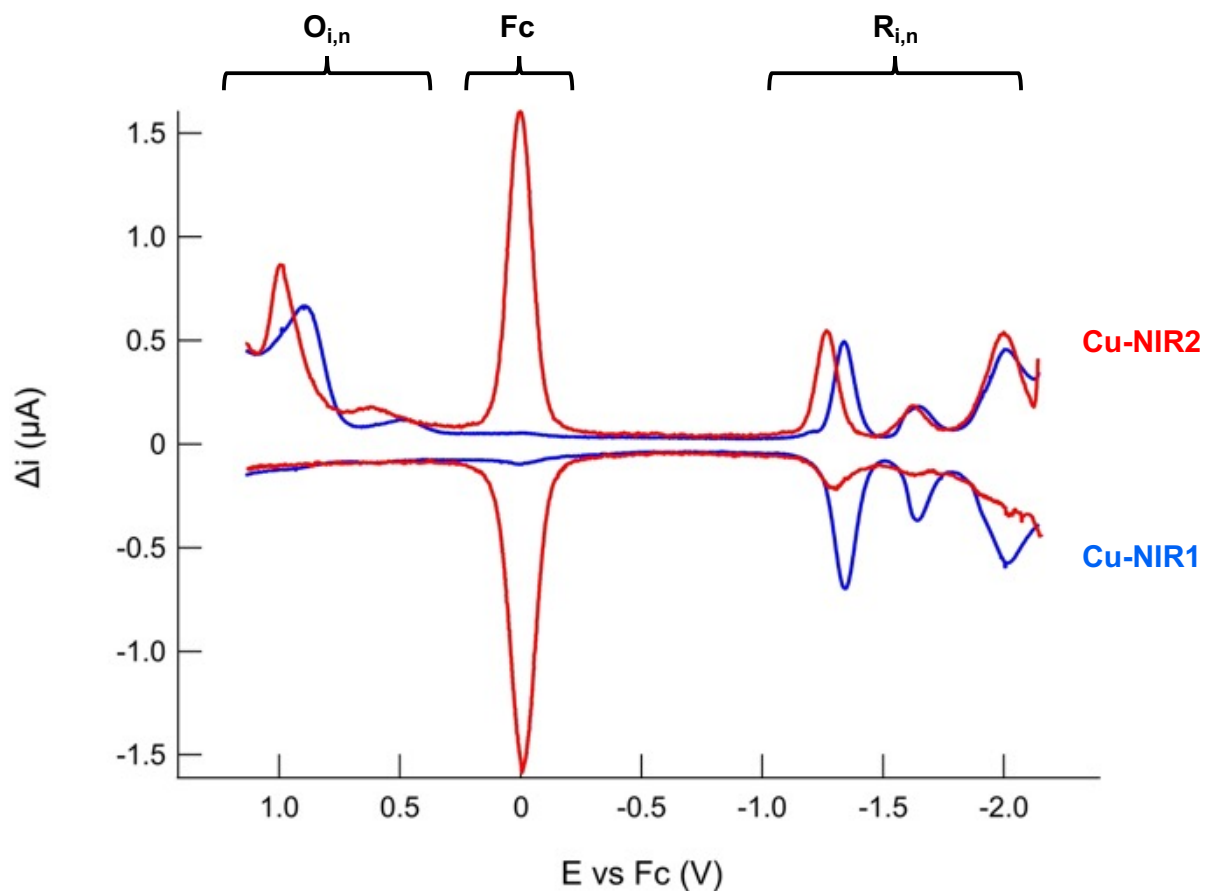
Figure S29. DPV copper complexes Cu-NIR1 (blue curve), Cu-NIR2 (red curve) and Ferrocene (Fc) at concentration of 1 mM carried out in CH_2Cl_2/0.1 M $TBPF_6$. Pulse width = 100 ms, Pulse heigh = 5 mV.
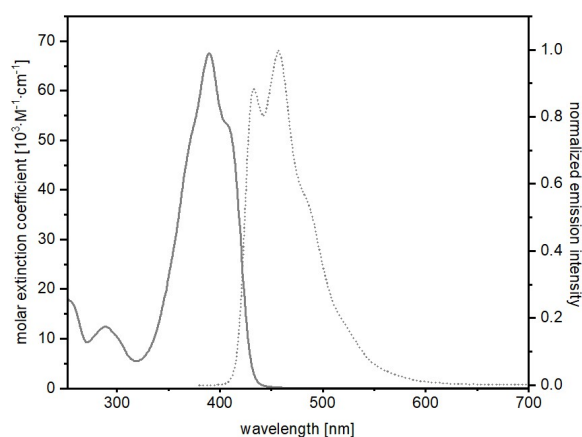
Figure S30. Electronic absorption (solid trace) and emission (dotted trace) spectra of pro-ligand **L1** recorded in dilute CH_2Cl_2 solution in air condition at room temperature upon excitation at λ_{exc} = 360 nm.
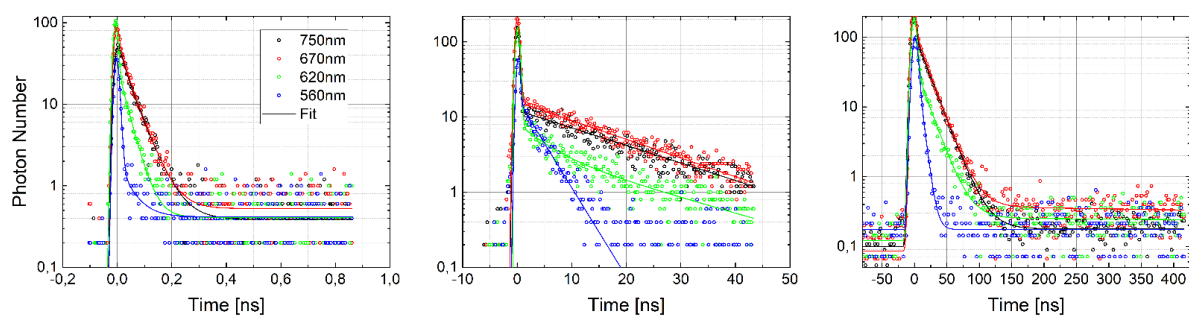
Figure S31. Kinetic traces obtained of complex **Cu-NIR2** for time ranges (A) 1 ns, (B) 50 ns and (C) 500 ns. Fitting curves obtained from data recorded for CH_2Cl_2 samples at concentration of 3×10^{-5} M at room temperature.
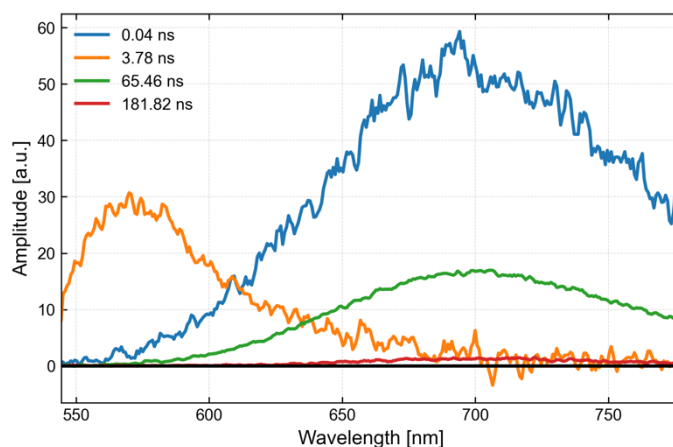
Figure 32. Decay Associated Emission Spectra (DAES) of lifetimes τ_2 to τ_5 as obtained from the global fit of the bi-metallic complex **Cu-NIR1**.
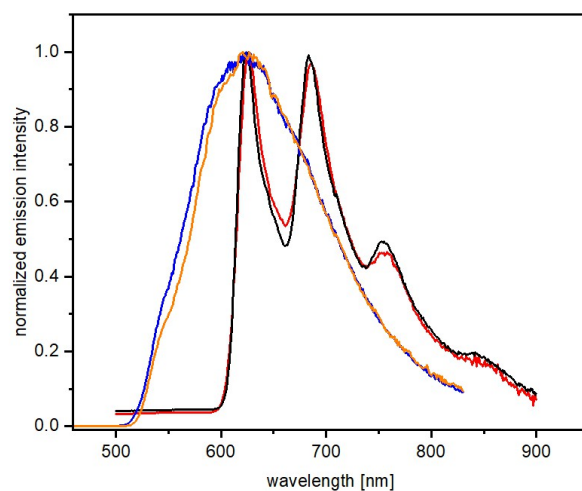
Figure S33. Emission spectra of dinuclear copper(I) complexes **Cu-NIR1** (red trace) and **Cu-NIR2** (black trace) and mononuclear **M1** (blue trace) and **M2** (orange trace) recorded in CH_2Cl_2 glassy matrix at 77 K upon excitation at λ_{exc} = 480 nm for **Cu-NIR1** and **Cu-NIR2** and at λ_{exc} = 425 nm for **M1** and **M2**.
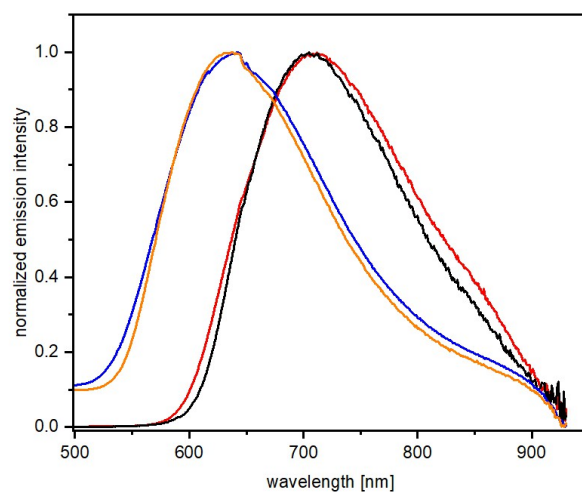
Figure S34. Emission spectra of dinuclear copper(I) complexes **Cu-NIR1** (red trace) and **Cu-NIR2** (black trace) and mononuclear **M1** (blue trace) and **M2** (orange trace) recorded in solid state as neat powder upon excitation at λ_{exc} = 480 nm.
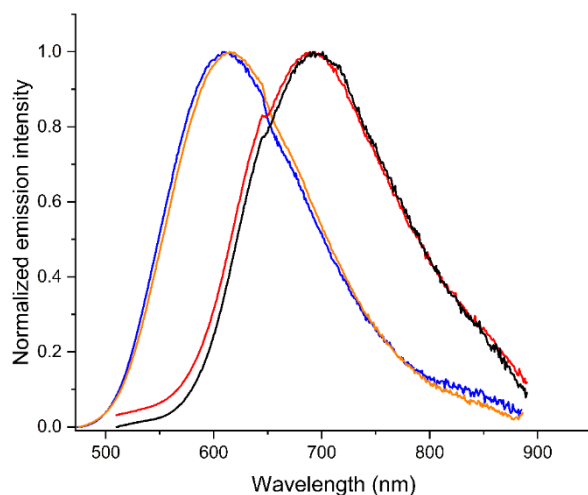
Figure S35. Emission spectra of PMMA thin-film samples at 10 wt.% doping of dinuclear copper(I) complexes **Cu-NIR1** (red trace) and **Cu-NIR2** (black trace) and mononuclear derivatives **M1** (blue trace) and **M2** (orange trace) recorded excitation at 480 nm for **NIR-Cu1** and **NIR-Cu2**, and at 455 nm for **M1** and **M2**.
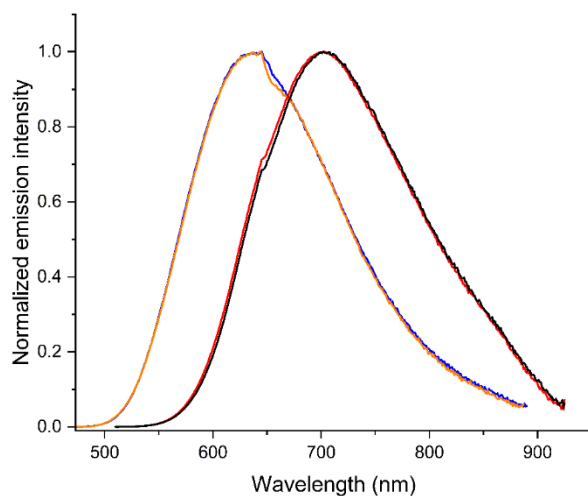
Figure S36. Emission spectra of thin-film blends with **complex**:[BMIM$^+$(PF6)$^-$] 80 wt.% : 20 wt.% for dinuclear copper(I) complexes **Cu-NIR1** (red trace) and **Cu-NIR2** (black trace) and mononuclear **M1** (blue trace) and **M2** (orange trace) recorded upon excitation at 480 nm for **NIR-Cu1** and **NIR-Cu2**, and at 455 nm for **M1** and **M2**.

Supplementary computational data

Supplementary discussion #2: ground state optimization of Cu-NIR1

In an attempt to quantify the distortion occurring in complex **Cu-NIR1** we defined the M-C_2-C_9 angle which is of 174.7° in free **4** and that reduces to 160° in the computed structure of **Cu-NIR1**. A less stable conformer was also found, being 0.094 eV less stable, in which one of π-stacking interaction with the pyridine rings is lost.
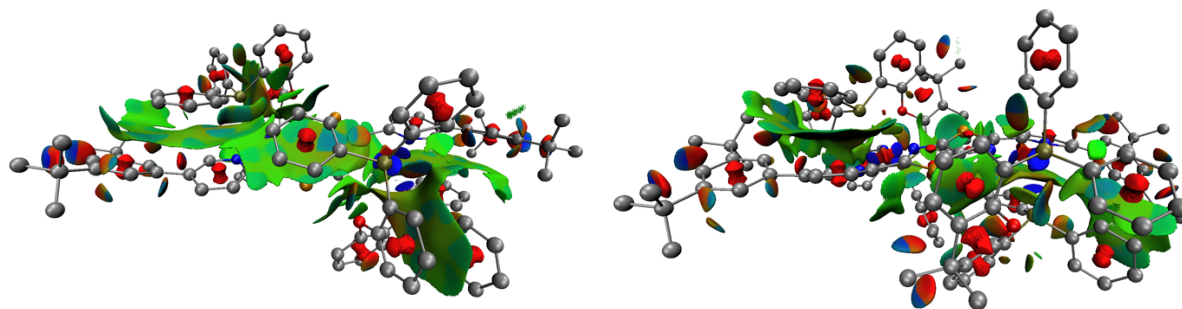
Figure S37. NCI analysis of the ground state structure of **Cu-NIR1** (*left*) and **Cu-NIR2** (*right*). See computational details for the procedure. Green, red and blue areas represent areas with attractive Van der Waals forces, steric hindrance and attractive electrostatic interactions, respectively. Hydrogens are omitted for clarity.
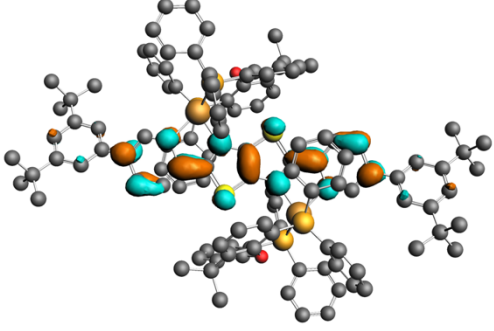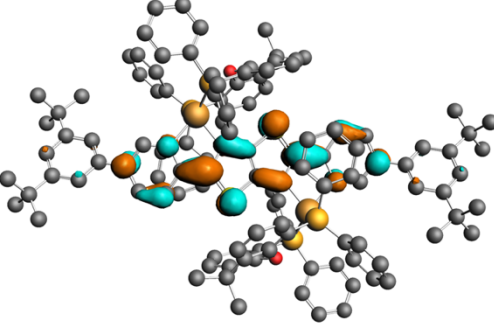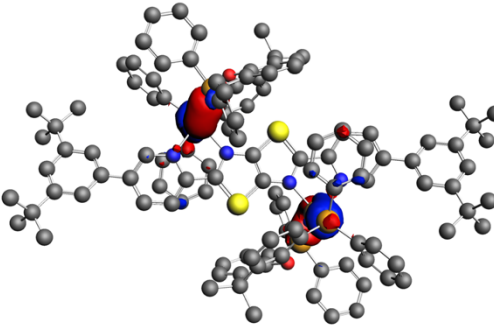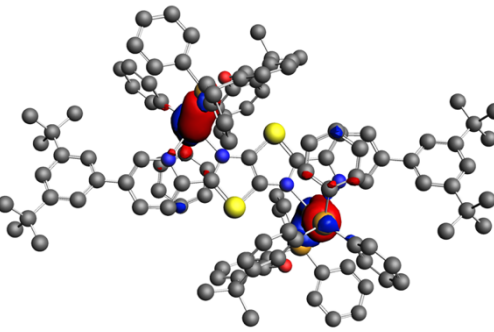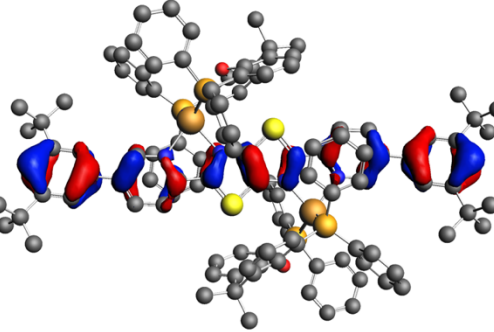
LUMO+1 -2.985 eV	
LUMO -3.893 eV	
HOMO -6.795 eV	
HOMO-1 -6.803 eV	
HOMO-2 -7.049 eV	

Figure S38. Nature and energies of the frontier orbitals **Cu-NIR2** complex.
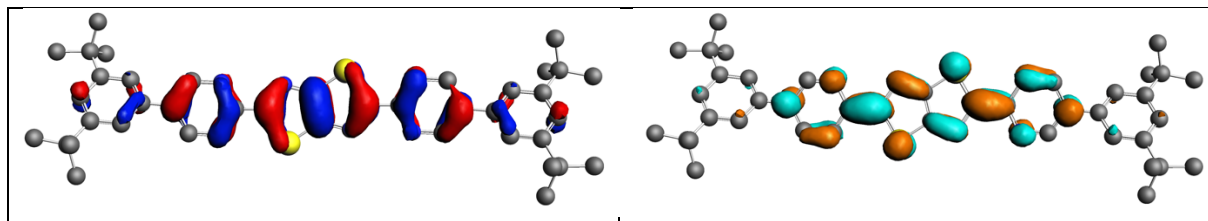
Figure S39. HOMO (*left*) and LUMO (*right*) of pro-ligand **L1**. Hydrogens are omitted for clarity.
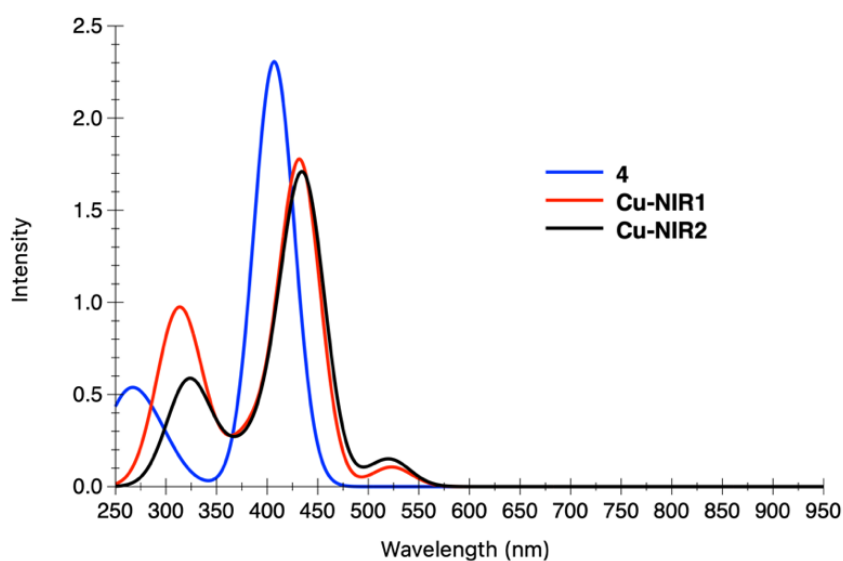
Figure S40. TD-DFT computed absorption spectra for compound **L1**, **Cu-NIR1** and **Cu-NIR** in CH_2Cl_2.
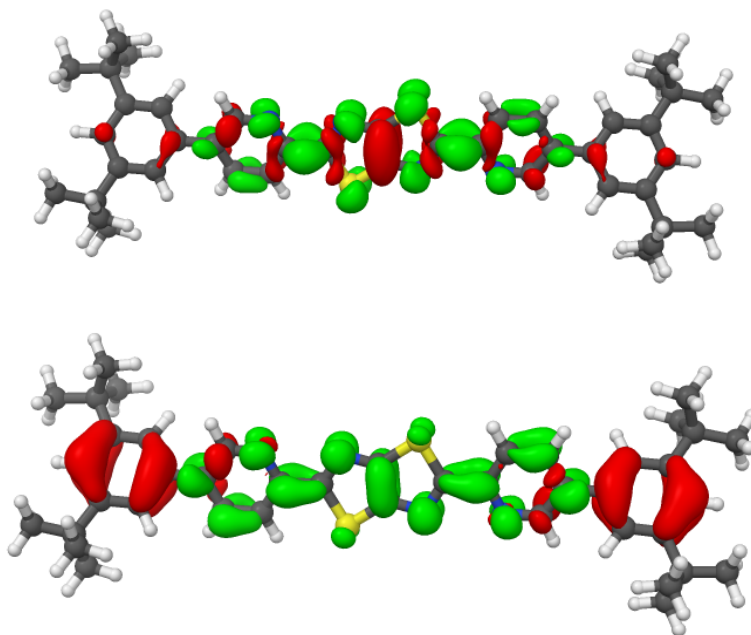
Figure S41. EDDMs for the $S_0 \rightarrow S_1$ (*top*) and $S_0 \rightarrow S_{13}$ (*bottom*) transition determined by difference between ground and excited state. Electronically enriched areas are in green and electronically impoverished areas are in red.

S33

Supplementary discussion #3: effect of conformation in ligand 4.

The study of the energy variation of the pro-ligand **L1** upon variation of the N_1-C_2-C_3-N_2 and C_4-C_5-C_6-C_7 dihedral angle was carried out (see Table S12). The energy variations are very small upon rotation (except when both C_4-C_5-C_6-C_7 dihedral angles are set to 0°) showing that **L1** is very flexible and can easily distort to maximize the interactions with the copper and the disphosphine ligand(s). Let us mention the consequences of the ligand **L1** flexibility. We have computed the absorption spectrum of the different rotamer of **L1** (Figure S42). Upon geometry variation, the main absorbing band computed at 407 nm varies from 353 nm for **L1_G** to 427 nm for **L1_A**.
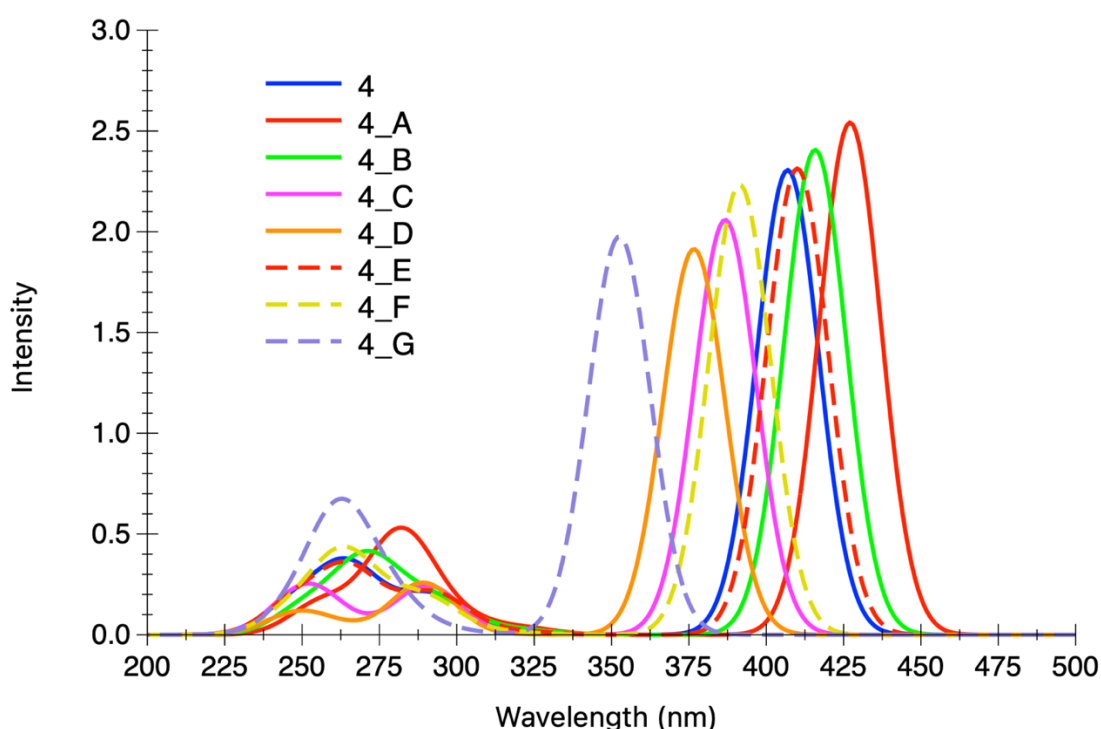
Figure S42. TD-DFT absorption spectrum computed for different rotamers of pro-ligand **L1**.

The emission wavelength for ligand **L1** is computed at 511 nm (S1 state) quite far from the experimental value of 457 nm (Table 1). This illustrates the difficulty to compute an emission wavelength on such flexible molecule. The emissive singlet of **L1** as the same nature as the S1 state fond in the absorption spectra (Figure S40). We again explore the sensitivity of the emission wavelength upon variation of the C_4-C_5-C_6-C_7 and N_1-C_2-C_3-N_2 torsion angles and of the $C_{2'}$-C_2-C_9 angle to mimic the distortion induced by the complexation for the latter. As expected, more planar is the structure more shift the emission wavelength towards the red (up to 532 nm for C_4-C_5-C_6-C_7 and $C_{4'}$-$C_{5'}$-$C_{6'}$-$C_{7'}$ torsion angles set to 0.0°, see Table S13). On the contrary, out-of-plane distortions through the torsion angles shifts the emission to the blue (454

nm when C_4-C_5-C_6-C_7 and $C_{4'}$-$C_{5'}$-$C_{6'}$-$C_{7'}$ torsion angles set to 90.0°, see Table S13). Surprisingly out-of-plane distortions by setting $C_{2'}$-C_2-C_9 angle to 140° (instead of roughly 180.0° in the fully optimized structure) shifts the emission wavelength towards the red though (533 nm) being not too destabilized, only 0.167 eV (3.8 kcal/mol) above the optimized structure of S1. Forcing the S-shape of the ligand by also setting the C_2-$C_{2'}$-$C_{9'}$ angle to 140° shifts the emission further to red (544 nm).
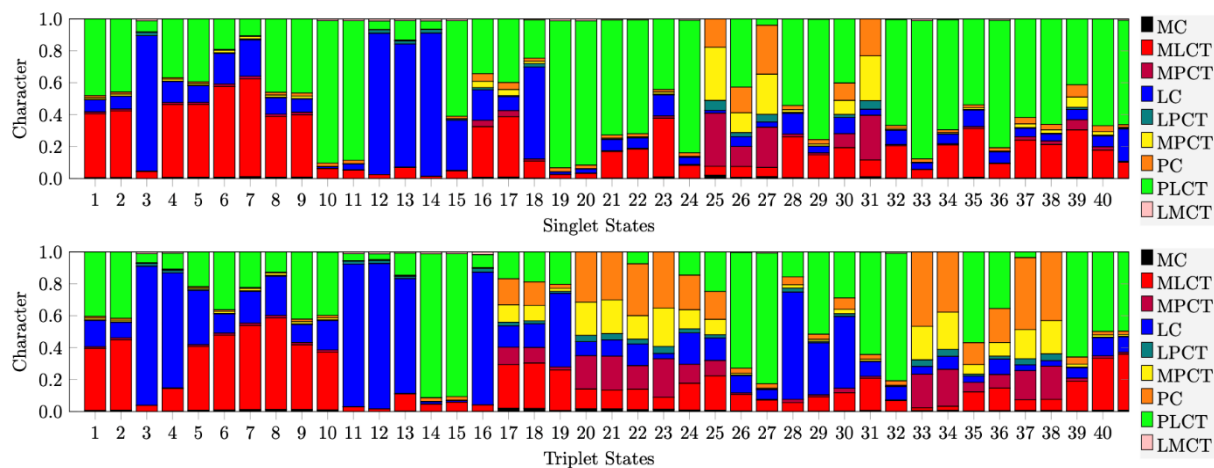
Figure S43. Theodore analysis of the **Cu-NIR1** complex at Franck-Condon geometry for singlet states (*top*) and triplet states (*bottom*). The complex is divided in free parts, the metal cations (M), the DPEPhos ligand (P) and the ligand **L1** (L).
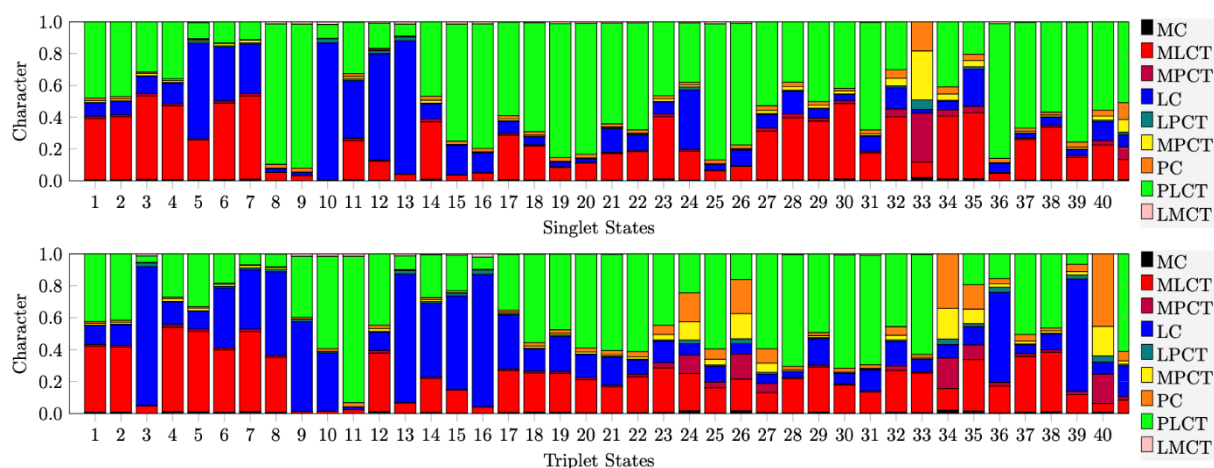
Figure S44. Theodore analysis of the **Cu-NIR2** complex at Franck-Condon geometry for singlet states (*top*) and triplet states (*bottom*). The complex is divided in free parts, the metal cations (M), the XantPhos ligand (P) and the ligand **L1** (L).
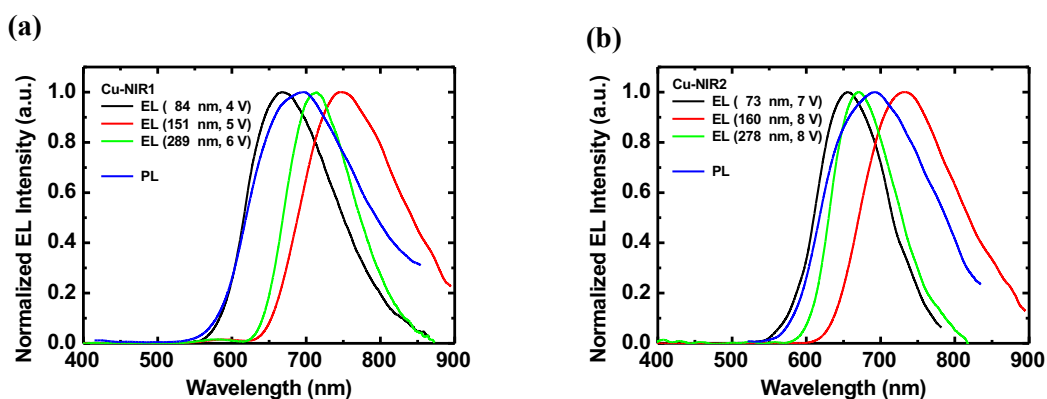
Figure S45. Thickness-dependent EL spectra of the LECs based on complexes (a) **Cu-NIR1** and (b) **Cu-NIR2**. The device thickness and bias voltage of each device are shown in the inset. The PL spectra of the emissive layers are also shown for comparison.
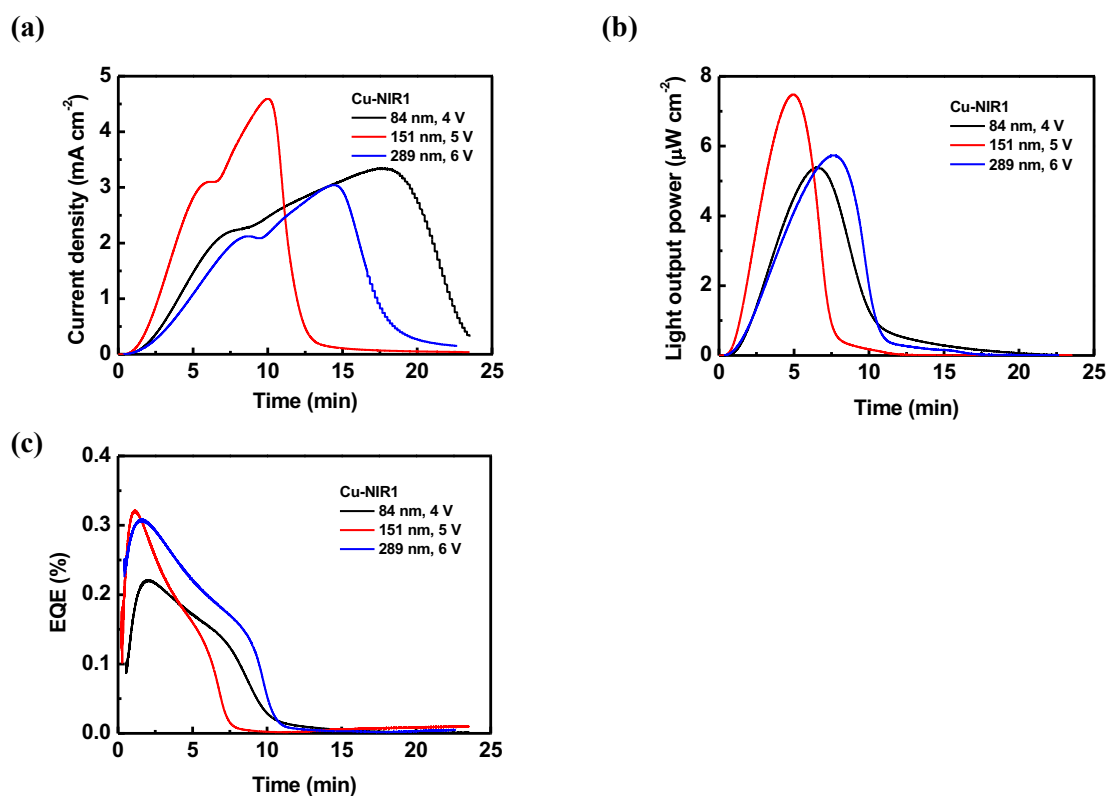
Figure S46. Time-dependent (a) current density, (b) light output power, and (c) EQE of the LECs based on complex **Cu-NIR1**. The device thickness and the bias voltage of each device are shown in the inset.

(a)

(b)

(c)
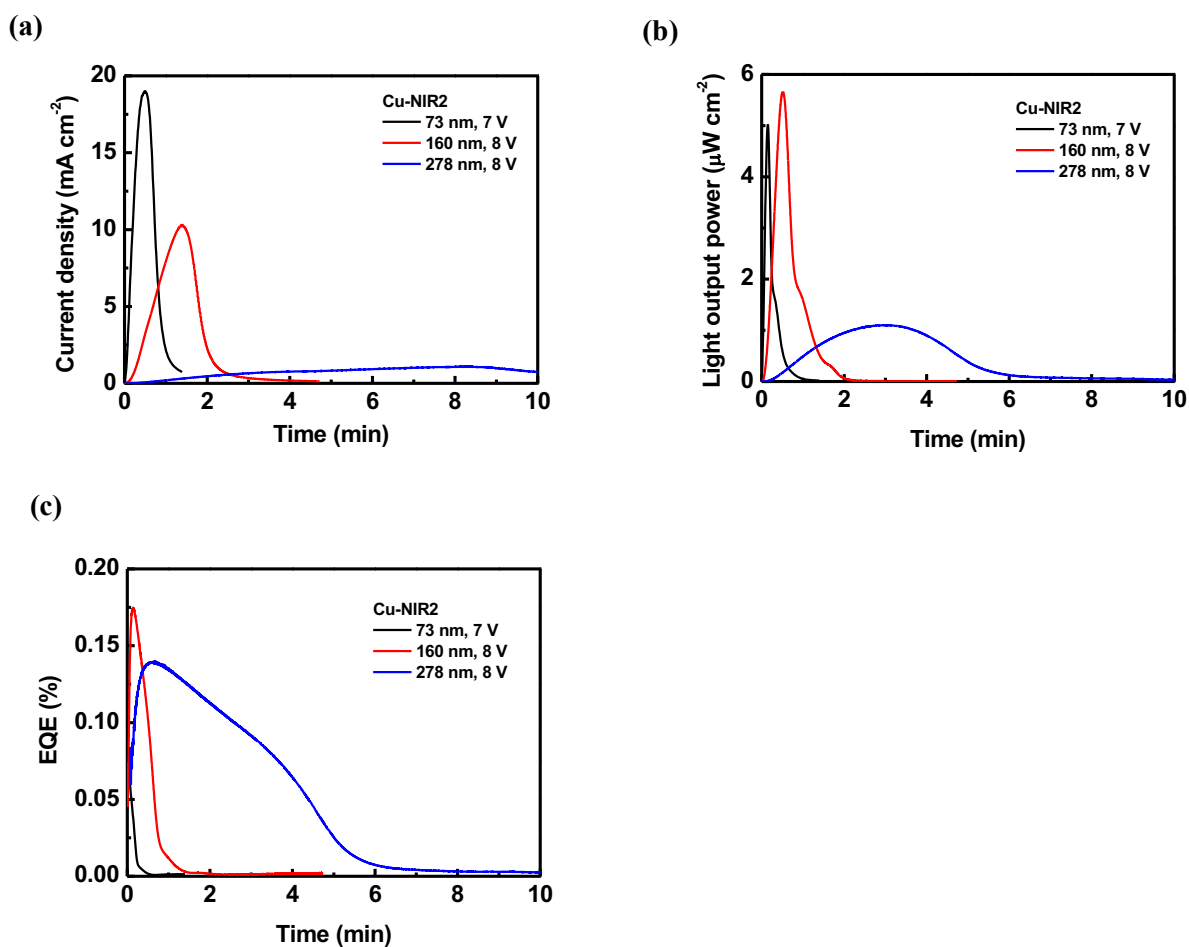
Figure S47. Time-dependent (a) current density, (b) light output power, and (c) EQE of the LECs based on complex **Cu-NIR2**. The device thickness and the bias voltage of each device are shown in the inset.

(a)

(b)
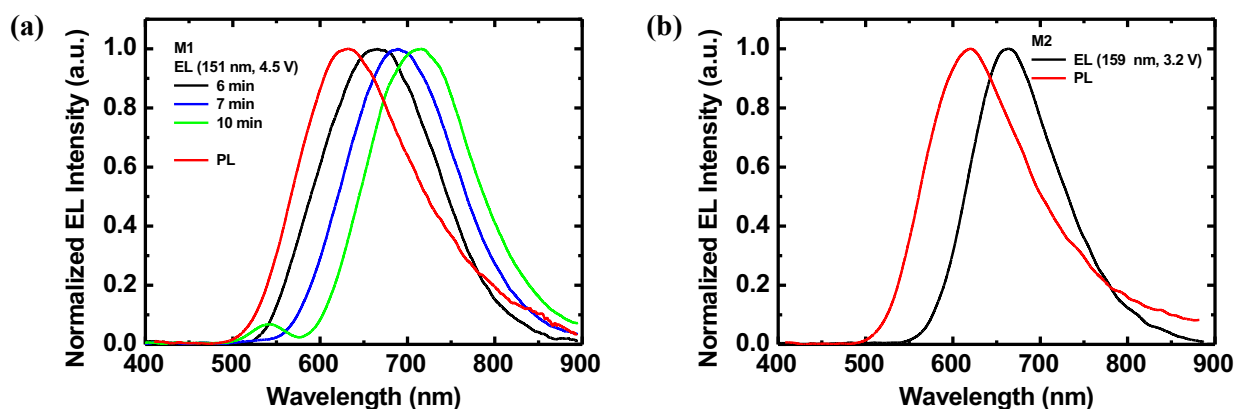
Figure S48. EL spectra of the LECs based on complexes (a) **M1** and (b) **M2**. The device thickness and bias voltage of each device are shown in the inset. The PL spectra of the emissive layers are also shown for comparison.
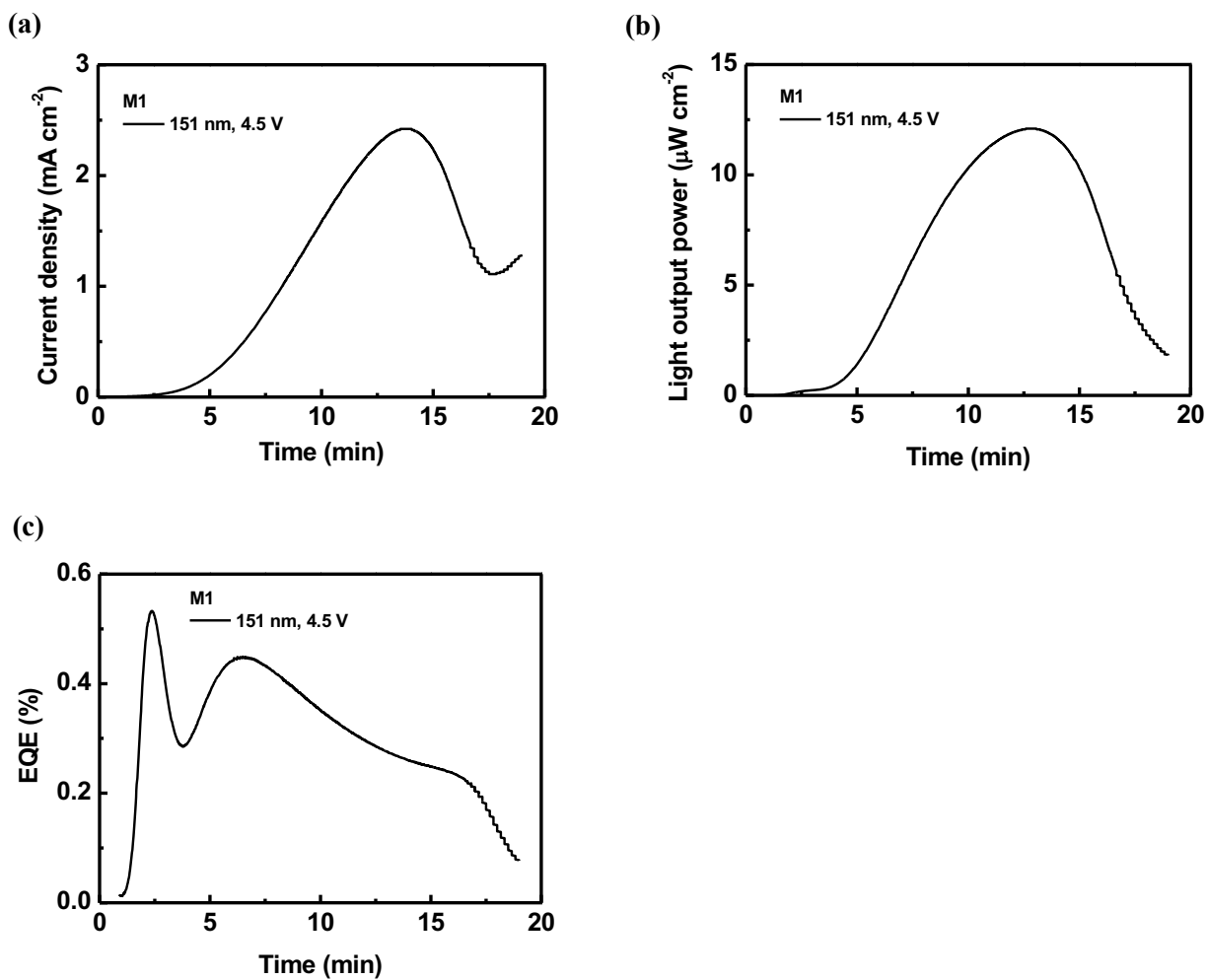
Figure S49. Time-dependent (a) current density, (b) light output power, and (c) EQE of the LECs based on complex **M1**. The device thickness and the bias voltage of each device are shown in the inset.
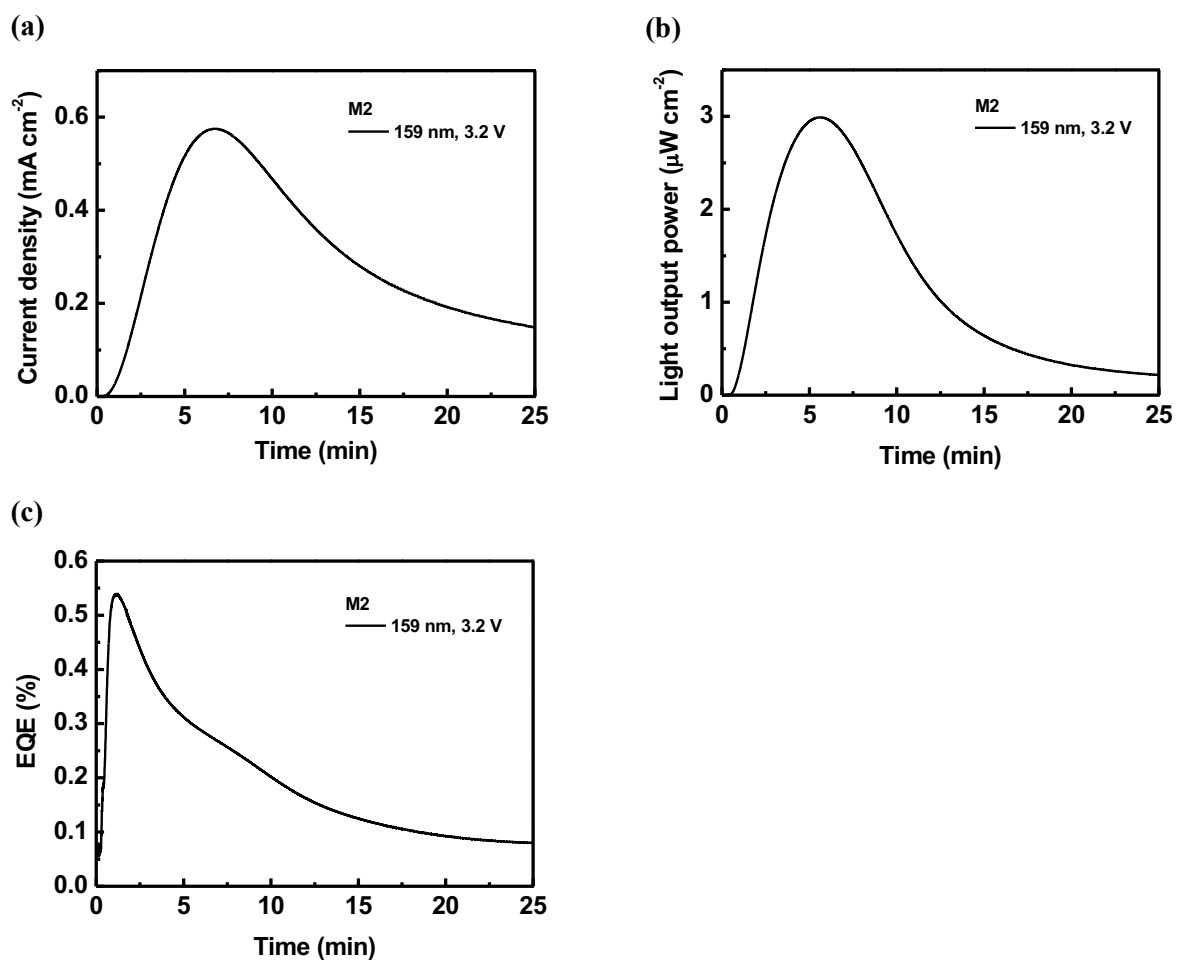
Figure S50. Time-dependent (a) current density, (b) light output power, and (c) EQE of the LECs based on complex **M2**. The device thickness and the bias voltage of each device are shown in the inset.

Complex YIr
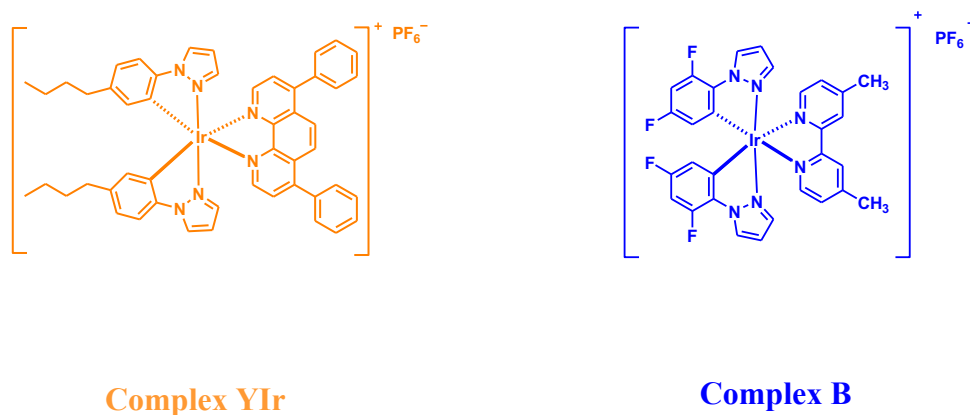
Complex B

Figure S51. Molecular structures of complexes **YIr** and **B**.
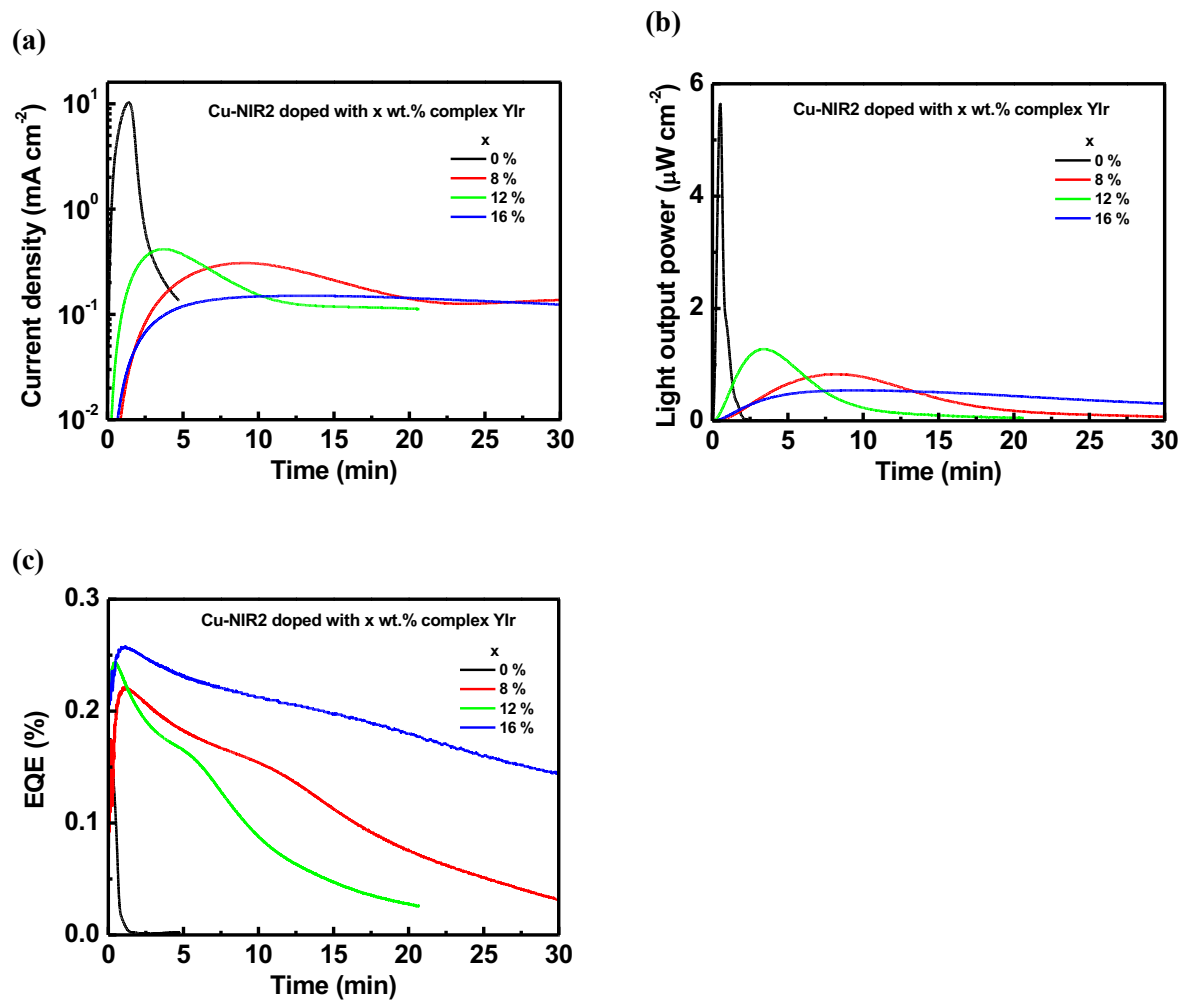
Figure S52. Time-dependent (a) current density, (b) light output power, and (c) EQE of the LECs based on complex **Cu-NIR2** doped with x wt.% complex **YIr**. The bias voltages for the LECs doped with 0, 8, 12, and 16 wt.% complex **YIr** are 8, 3, 3, and 2.5 V, respectively.

Supplementary discussion #4

Constant-current operation was performed for the white LECs employing complex **B** as the host to obtain better device efficiency.[48] The time-dependent normalized EL spectra of the white LECs based on complex **B** doped with 0.6 wt.% complex **Cu-NIR1** are depicted in Figure S53a. The EL emission from complex **Cu-NIR1** was indeed blue-shifted to the deep-red spectra region (λ_{max} = *ca.* 676 nm) upon dilute doping. Initially, the EL spectrum of the white LEC was predominantly blue-green and the percentage of red emission increased with time. It is related to the time-dependent device voltage under the constant-current operation (see below). Finally, the Commission Internationale de l'Éclairage (CIE) 1931 coordinate of the stabilized EL spectra approached the equal-energy point (0.33, 0.33) (Figure S53b).

The time-dependent voltage, brightness, and EQE of the white LEC based on complex **B** doped with 0.6 wt.% complex **Cu-NIR1** are shown in Figure S54. When the LEC was applied with a constant current, the device voltage is initially high due to the poor carrier injection into the undoped emissive layer. With the gradually formed electrochemically doped layers, the device voltage then decreased due to reduced resistance. Initially higher device voltage facilitated carriers to be injected into the higher-gap host, rendering a higher percentage of host emission (*cf.* EL at 6 min, Figure S53a).[49] Subsequently reduced device voltage lead to more significant carrier trapping on the lower-gap guest and thus enhanced guest emission can be measured (*cf.* EL after 10 min, Figure S53a).[50] Finally, the device voltage reached a steady-state value after the *p*-i-*n* structure was fully established. During the formation of electrochemically doped layers, the balance of carrier injection can be improved gradually such that the brightness and the EQE increased with time under a constant current. After reaching the peak value, the brightness and the EQE decreased with time gradually due to the material degradation and/or the exciton quenching by the doped layers.
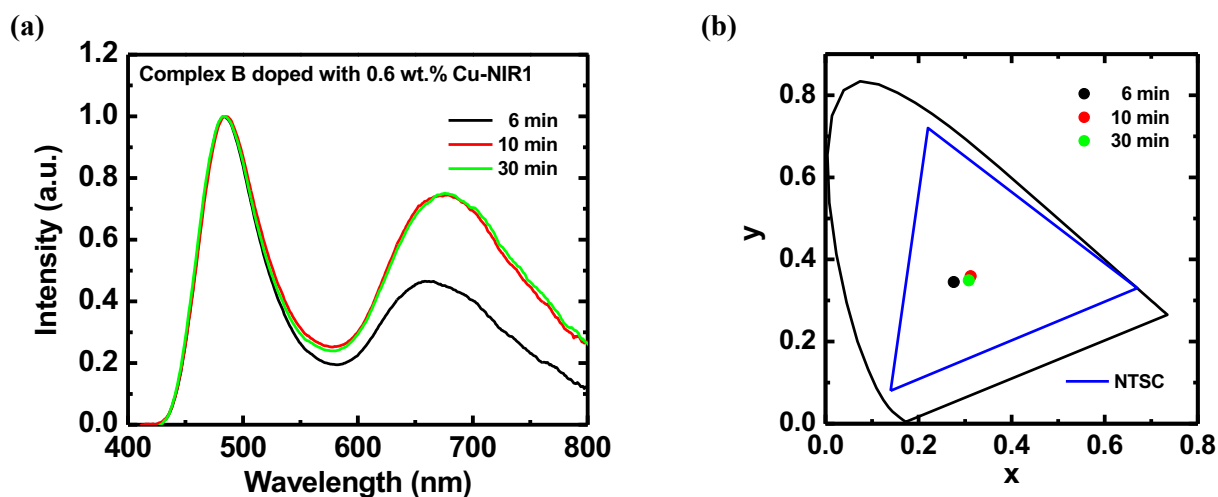
Figure S53. Time-dependent (a) normalized EL spectra and (b) corresponding CIE 1931 coordinates of the white LECs based on complex **B** doped with 0.6 wt.% **Cu-NIR1** under a constant current of 0.2 μA.
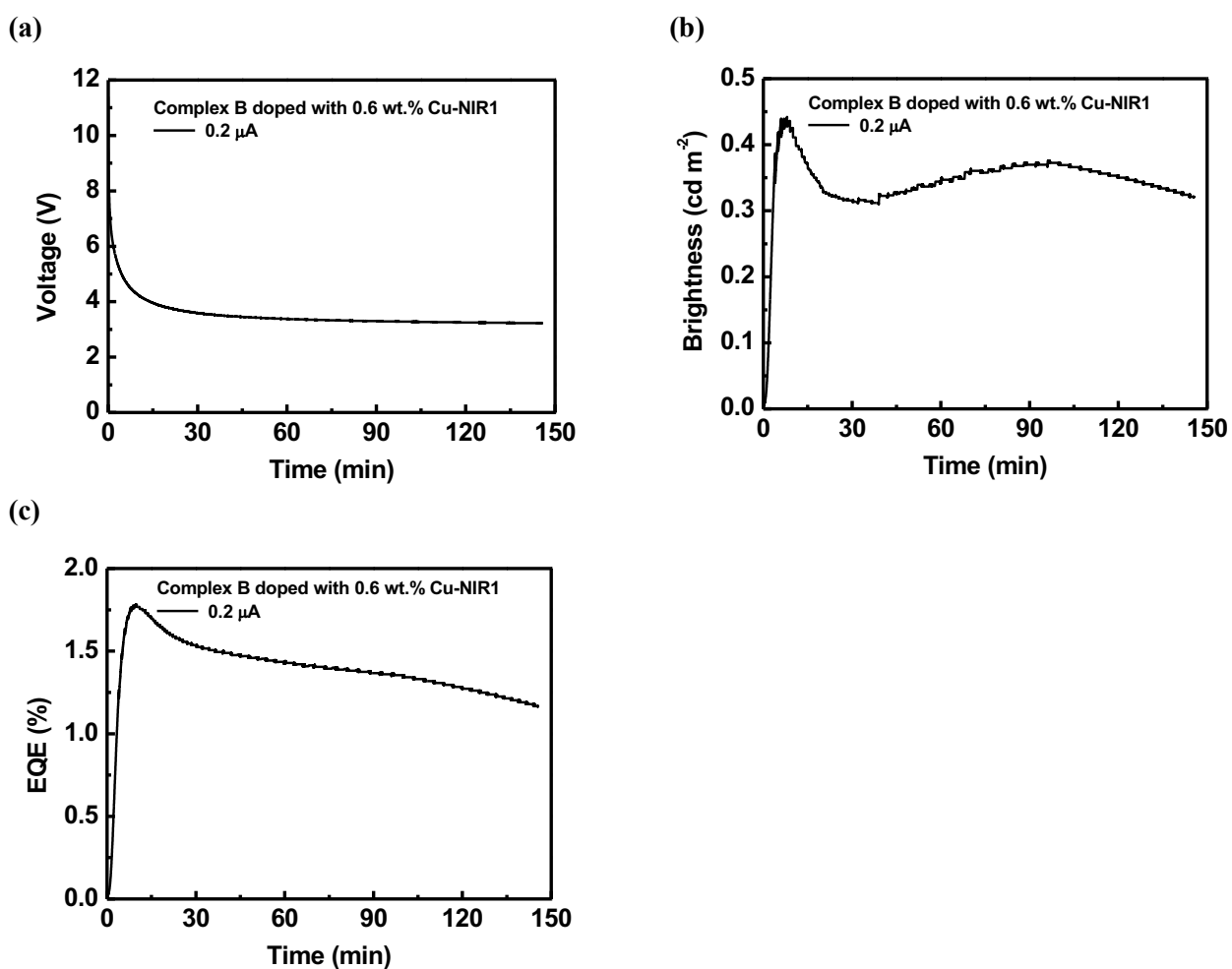
Figure S54. Time-dependent (a) voltage, (b) brightness, and (c) EQE of the white LECs based on complex **B** doped with 0.6 wt.% **Cu-NIR1** under a constant current of 0.2 μA.

S43

Supplementary Tables

Table S1. Crystal data and structure refinement for compound **L1** (CCDC 2251642).

Identification code	e5086
Chemical formula	$C_{42}H_{48}N_4S_2$
Formula weight	672.96 g/mol
Temperature	173(2) K
Wavelength	0.71073 Å
Crystal system, space group	monoclinic ,P 1 21/c 1
Unit cell dimensions	a = 11.3626(5) Å $\quad$ α = 90°
	b = 14.8002(7) Å $\quad$ β = 105.505(2)°
	c = 11.2088(5) Å $\quad$ γ = 90°
Volume	1816.37(14) Å^3
Z, Calculated density	2, 1.230 g/cm^3
Absorption coefficient	0.182 mm^{-1}
F(000)	720
Crystal size	0.080 x 0.100 x 0.110 mm
Theta range for data collection	1.86 to 27.98°
Limiting indices	-14<=h<=15, -19<=k<=19, -14<=l<=14
Reflections collected / unique	60039 / 4356 [R(int) = 0.0772]
Completeness to theta =	13.783 $\quad$ 99.5%
Max. and min. transmission	0.7316 and 0.7075
Refinement method	Full-matrix least-squares on F^2
Data / restraints / parameters	4356 / 0 / 223
Goodness-of-fit on F^2	1.151
Final R indices [I>2sigma(I)]	R1 = 0.0548, wR2 = 0.1505
R indices (all data)	R1 = 0.0663, wR2 = 0.1576
Extinction coefficient	n/a
Largest diff. peak and hole	0.460 and -0.402 eÅ^{-3}

Table S2. Crystal data and structure refinement for compound **M1** (CCDC 2251640).

Identification code	emmaj220928
Empirical formula	C65 H59 Cl9 Cu F6 N2 O P3 S
	C62 H56 Cu N2 O P2 S, F6 P, 3(C H Cl3)
Formula weight	1505.70
Temperature	120(2) K
Wavelength	0.71073 Å
Crystal system, space group	Triclinic, P -1
Unit cell dimensions	a = 12.5958(5) Å α = 78.9200(10)°
	b = 15.4279(5) Å β = 78.9480(10)°
	c = 18.9815(7) Å γ = 74.9080(10)°
Volume	3455.7(2) Å^3
Z, Calculated density	2, 1.447 Mg/m^3
Absorption coefficient	0.822 mm^{-1}
F(000)	1536
Crystal size	0.220 x 0.200 x 0.100 mm
Theta range for data collection	1.974 to 27.974°
Limiting indices	-16<=h<=16, -20<=k<=20, -25<=l<=25
Reflections collected / unique	151814 / 16619 [R(int) = 0.0508]
Completeness to theta =	25.242 99.9%
Absorption correction	Semi-empirical from equivalents
Max. and min. transmission	0.7456 and 0.6820
Refinement method	Full-matrix least-squares on F^2
Data / restraints / parameters	16619 / 6 / 817
Goodness-of-fit on F^2	1.029
Final R indices [I>2sigma(I)]	R$_1$ = 0.0708, wR^2 = 0.1930
R indices (all data)	R$_1$ = 0.0863, wR^2 = 0.2086
Extinction coefficient	n/a
Largest diff. peak and hole	1.803 and -1.462 e Å^{-3}

Table S3. Crystal data and structure refinement for compound **M2** (CCDC 2251641).

Identification code	emmaj221002
Empirical formula	C133 H126 Cu2 F12 N4 O2 P6 S2
	2(C65 H60 Cu N2 O P2 S), 2(F6 P), C3 H6
Formula weight	2417.39
Temperature	120(2) K
Wavelength	0.71073 Å
Crystal system, space group	Triclinic, P -1
Unit cell dimensions	a = 10.7027(4) Å α = 95.457(2)°
	b = 14.2315(7) Å β = 96.967(2)°
	c = 21.1240(10) Å γ = 105.113(2)°
Volume	3056.2(2) Å^3
Z, Calculated density	1, 1.313 Mg/m^3
Absorption coefficient	0.532 mm^{-1}
F(000)	1256
Crystal size	0.200 x 0.180 x 0.160 mm
Theta range for data collection	1.960 to 27.944°
Limiting indices	-14<=h<=14, -18<=k<=18, -27<=l<=27
Reflections collected / unique	247658 / 14654 [R(int) = 0.0749]
Completeness to theta =	25.242 99.8%
Absorption correction	Semi-empirical from equivalents
Max. and min. transmission	0.7456 and 0.7137
Refinement method	Full-matrix least-squares on F^2
Data / restraints / parameters	14654 / 0 / 747
Goodness-of-fit on F^2	1.040
Final R indices [I>2sigma(I)]	R_1 = 0.0418, wR^2 = 0.1169
R indices (all data)	R_1 = 0.0546, wR^2 = 0.1273
Extinction coefficient	n/a
Largest diff. peak and hole	0.902 and -0.625 e Å^{-3}

Table S4. Crystal data and structure refinement for compound **Cu-NIR1** (CCDC 2251525).

Identification code	e5114a_a_sq
Empirical formula	C114 H104 Cu2 F12 N4 O2 P6 S2, solvent 'C114 H104 Cu2 N4 O2 P4 S2, 2(F6 P),solvent'
Formula weight	2167.03
Temperature	173(2) K
Wavelength	0.71073 Å
Crystal system, space group	Triclinic, P -1
Unit cell dimensions	a = 10.7779(7) Å α = 83.582(3)°
	b = 14.2458(9) Å β = 81.991(3)°
	c = 20.1112(13) Å γ = 86.694(3)°
Volume	3035.8(3) Å^3
Z, Calculated density	1, 1.185 Mg/m^3
Absorption coefficient	0.528 mm^{-1}
F(000)	1120
Crystal size	0.150 x 0.150 x 0.100 mm
Theta range for data collection	1.679 to 27.827°
Limiting indices	-13<=h<=14, -18<=k<=18, -26<=l<=24
Reflections collected / unique	38578 / 13442 [R(int) = 0.0688]
Completeness to theta =	25.242 95.5%
Absorption correction	Semi-empirical from equivalents
Max. and min. transmission	0.7456 and 0.6308
Refinement method	Full-matrix least-squares on F^2
Data / restraints / parameters	13442 / 18 / 653
Goodness-of-fit on F^2	1.022
Final R indices [I>2s(I)]	R_1 = 0.0676, wR^2 = 0.1670
R indices (all data)	R_1 = 0.0991, wR^2 = 0.1857
Extinction coefficient	n/a
Largest diff. peak and hole	1.188 and -0.672 e Å^{-3}

Table S5. Crystal data and structure refinement for compound **Cu-NIR2** (CCDC 2251639).

Identification code	e5112a_a_sq
Empirical formula	C132 H140 Cl8 Cu2 F12 N4 O4 P6 S2, solvent
	'C120 H112 Cu2 N4 O2 P4 S2,2(F6P),2(C4H10O),4(CH2Cl2),solvent'
Formula weight	2735.09
Temperature	173(2) K
Wavelength	0.71073 Å
Crystal system, space group	Triclinic, P -1
Unit cell dimensions	a = 15.1464(9) Å $\quad$ α = 87.582(4)º
	b = 16.1342(9) Å $\quad$ β = 65.353(3)º
	c = 16.5116(10) Å $\quad$ γ = 65.691(3)º
Volume	3301.2(4) Å^3
Z, Calculated density	1, 1.376 Mg/m^3
Absorption coefficient	0.659 mm^{-1}
F(000)	1416
Crystal size	0.150 x 0.130 x 0.130 mm
Theta range for data collection	1.374 to 28.074º
Limiting indices	-19<=h<=19, -21<=k<=21, -21<=l<=21
Reflections collected / unique	221586 / 14659 [R(int) = 0.1298]
Completeness to theta =	25.242 94.4%
Absorption correction	Semi-empirical from equivalents
Max. and min. transmission	0.7374 and 0.6444
Refinement method	Full-matrix least-squares on F^2
Data / restraints / parameters	14659 / 0 / 780
Goodness-of-fit on F^2	1.044
Final R indices [I>2sigma(I)]	R_1 = 0.1088, wR^2 = 0.3202
R indices (all data)	R_1 = 0.1431, wR^2 = 0.3525
Extinction coefficient	0.020(2)
Largest diff. peak and hole	3.339 and -1.495 e Å^{-3}

Table S6. Lifetimes obtained from the global fit for degassed CH_2Cl_2 samples of complexes **NIR-Cu1, NIR-Cu2**, **M1** and **M2**. Lifetimes marked with "–" were not found by the fitting routine. A fifth yet unresolved lifetime was needed for the 500 ns time range data.

Sample		τ_1 [ps]	τ_2 [ps]	τ_3 [ns]	τ_4 [ns]	τ_5 [ns]
Cu-NIR1	750 nm	–	39 ± 0.4	–	63 ± 3	> 100
	670 nm	20 ± 3	46 ± 5	3.8 ± 1.8	68 ± 2	> 100
	620 nm	10.4 ± 0.8	38 ± 3	3.8 ± 0.5	61 ± 9	> 100
	560 nm	10.3 ± 0.3	–	4.0 ± 0.1	–	> 100
Cu-NIR2	Glob. fit	–	45	3	17	∞
M1	Glob. fit	–	30	2.3	320	-
M2	Glob. fit	–	32	2.6	275	-

Table S7. Photophysical data recorded for complexes **NIR-Cu1**, **NIR-Cu2**, **M1** and **M2** in solid state as neat powders.

compound	λ_{em} [nm]	PLQY (%)	τ [µs]	τ_{ave} [µs]
Cu-NIR1	712	1	5.44 (12%) 0.96 (32%) 2.25 (56%)	3.1
Cu-NIR2	705	1	0.89 (38%) 2.44 (50%) 5.74 (11%)	3.2
M1	643	3	4.85 (32%) 1.96 (68%)	3.5
M2	637	3	1.84 (71%) 5.04 (29%)	3.5

Table S8. Photophysical data recorded for thin film samples of complexes **NIR-Cu1**, **NIR-Cu2**, **M1** and **M2** in PMMA 10 wt.% doping and in **complex** : [BMIM$^+$(PF$_6$)$^-$] blended at 80:20 wt.%.

Compound	PMMA 10 wt.% doping			complex:[BMIM$^+$(PF$_6$)$^-$] 80:20 wt.% blend		
	λ_{em} [nm]	PLQY (%)	τ^a [μs]	λ_{em} [nm]	PLQY (%)	τ^a [μs]
Cu-NIR1	692	0.5%	3.4 (55%) 14.7 (36%) [11.8]	702	1.4%	1.4 (55%) 5.8 (35%) [4.7]
Cu-NIR2	696	0.4%	9.9 (33%) 2.1 (59%) [7.7]	705	0.9%	1.4 (58%) 6.1 (35%) [4.8]
M1	611	5.5%	4.5 (61%) 15.8 (36%) [12.1]	636	3.3%	2.8 (46%) 0.9 (45%) [2.3]
M2	616	4.8%	4.4 (62%) 15.3 (34%) [11.5]	637	3.2%	1.4 (38%) 3.8 (54%) [3.3]

^{a} values in brackets correspond to average lifetime.

Table S9. Comparison of geometrical parameters obtained experimentally (X-ray) and theoretically at the GS, T$_{1a}$ and T$_{1b}$ state for complex **Cu-NIR1**. Distances, angles and dihedral angle are given in [Å] and [°] and [°], respectively. 1) structure optimized starting from X-ray structure. 2) lowest conformer found. The dihedral angles D1 and D2 are the angle between the Cu-N1-N2 and Cu-P-P or Cu-N1'-N2' and Cu-P'-P' planes respectively.

	X-ray	GS^1	GS^2	T$_{1a}$	T$_{1b}$
Cu-N1	2.100	2.173	2.216	1.973	2.092
Cu-N2	2.067	2.070	2.058	2.042	2.080
Cu-P	2.244	2.262	2.259	2.316	2.265
Cu-P	2.232	2.219	2.220	2.297	2.224
N1-C2-C3-N2	-6.6	-23.1	-23.3	-7.3	-13.3
C4-C5-C6-C7	-45.7	-41.7	-23.8	-40.0	-20.9
C2'-C2-C9	168.4	163.4	160.0	149.8	151.6
D1	85.9	81.9	78.6	63.5	78.6
Cu-N1'	2.100	2.098	2.216	2.169	2.081
Cu-N2'	2.067	2.071	2.058	2.071	2.078
Cu-P'	2.244	2.237	2.259	2.256	2.240
Cu-P'	2.232	2.198	2.220	2.226	2.201
N1'-C2'-C3'-N2'	6.6	7.4	23.3	21.2	4.7
C4'-C5'-C6'-C7'	45.7	37.2	23.8	27.3	35.9
C2-C2'-C9'	168.4	163.6	160.0	159.0	164.8
D2	85.9	84.7	78.6	78.6	85.5

Table S10. Comparison of geometrical parameters obtained experimentally (X-ray) and theoretically at the GS, T_{1a} and T_{1b} state for complex **Cu-NIR2**. Distances, angles and dihedral angle are given in [Å] and [°] and [°], respectively. The dihedral angles D1 and D2 are the angle between the Cu-N1-N2 and Cu-P-P or Cu-N1'-N2' and Cu-P'-P' planes respectively.

	X-ray	GS	T_{1a}	T_{1b}
Cu-N1	2.072	2.094	2.044	2.124
Cu-N2	2.097	2.110	1.987	2.085
Cu-P	2.275	2.265	2.290	2.290
Cu-P	2.226	2.208	2.385	2.226
N1-C2-C3-N2	-8.9	-8.7	1.1	-5.5
C4-C5-C6-C7	15.5	39.2	31.8	32.6
C2'-C2-C9	169.1	160.7	144.7	147.6
D1	83.6	86.0	73.0	83.1
Cu-N1'	2.072	2.094	2.095	2.102
Cu-N2'	2.097	2.110	2.100	2.103
Cu-P'	2.275	2.265	2.274	2.273
Cu-P'	2.226	2.208	2.208	2.220
N1'-C2'-C3'-N2'	8.9	8.7	9.3	9.1
C4'-C5'-C6'-C7'	-15.5	-39.2	-40.3	-31.8
C2-C2'-C9'	169.1	160.7	163.0	159.9
D2	83.6	86.0	84.2	81.1

Table S11. Absorption transition energies [in eV] and wavelength [in nm] along with the corresponding oscillator strength computed for compound **L1**.

state	E_{abs} [eV]	λ_{abs} [nm]	f_{osc}
S1	3.047	407	2.31E+00
S2	3.775	328	8.00E-06
S3	3.846	322	1.11E-02
S4	3.848	322	1.32E-04
S5	3.947	314	1.51E-07
S6	4.040	307	1.15E-02
S7	4.150	299	3.44E-06
S8	4.196	295	1.34E-01
S9	4.347	285	7.39E-02
S10	4.409	281	2.62E-02
S11	4.431	280	5.13E-05
S12	4.580	271	1.37E-07
S13	4.682	265	3.01E-01
S14	4.715	263	2.71E-02
S15	4.719	263	1.89E-04
S16	4.839	256	1.80E-06
S17	4.941	251	7.68E-05
S18	5.013	247	1.45E-01
S19	5.015	247	6.18E-04
S20	5.030	246	4.50E-03

Table S12. Energy variation as function of the N_1-C_2-C_3-N_2 and C_4-C_5-C_6-C_7 dihedral angles of compound **L1** in in [eV] and [kcal mol^{-1}]. See Scheme S3 for atom labelling.

Structure	N_1-C_2-C_3-N_2	$N_{1'}$-$C_{2'}$-$C_{3'}$-$N_{2'}$	C_4-C_5-C_6-C_7	$C_{4'}$-$C_{5'}$-$C_{6'}$-$C_{7'}$	ΔE [eV]	ΔE [kcal mol^{-1}]
L1_A	12.0	12.0	0.0	0.0	0.325	7.5
L1_B	12.0	12.0	0.0	44.0	0.165	3.8
L1	12.0	12.0	44.0	44.0	0.006	0.1
L1_C	12.0	12.0	44.0	90.0	0.084	1.9
L1_D	12.0	12.0	90.0	90.0	0.164	3.8
L1_E	0.0	0.0	44.0	44.0	0.006	0.1
L1_F	23.0	23.0	44.0	44.0	0.000	0.0
L1_G	45.0	45.0	44.0	44.0	0.054	1.2

Table S13. Energy variation as a function of the N_1-C_2-C_3-N_2 and C_4-C_5-C_6-C_7 dihedral angles and of the $C_{2'}$-C_2-C_9 angle of **L1** and associated emission wavelength after partial geometry relaxation. See Scheme S3 for atom labelling. Energies are given in [eV] and [kcal mol^{-1}].

Constraint 1		Constraint 2		ΔE [eV]	ΔE [kcal mol^{-1}]	λ_{em} [nm]
Parameter	Value	Parameter	Value			
N_1-C_2-C_3-N_2	25.0			0.068	1.6	501
C_4-C_5-C_6-C_7	0.0			0.062	1.4	520
C_4-C_5-C_6-C_7	90.0			0.184	4.3	487
C_4-C_5-C_6-C_7	0.0	$C_{4'}$-$C_{5'}$-$C_{6'}$-$C_{7'}$	0.0	0.119	2.8	532
C_4-C_5-C_6-C_7	90.0	$C_{4'}$-$C_{5'}$-$C_{6'}$-$C_{7'}$	90.0	0.422	9.7	454
$C_{2'}$-C_2-C_9	140.0			0.167	3.8	533
$C_{2'}$-C_2-C_9	140.0	C_2-$C_{2'}$-$C_{9'}$	140.0	0.363	8.4	544

Table S14. Absorption transition energies in [eV] and wavelength in [nm] along with the corresponding oscillator strength computed for complexes **Cu-NIR1** and **Cu-NIR2**.

	Cu-NIR1				**Cu-NIR2**		
	E_{abs} [eV]	λ_{abs} [nm]	f_{osc}		E_{abs} [eV]	λ_{abs} [nm]	f_{osc}
S1	2.370	523	1.06E-01		2.361	525	9.43E-02
S2	2.407	515	0.00E+00		2.421	512	6.33E-02
S3	2.866	433	1.73E+00		2.694	460	1.17E-02
S4	2.975	417	0.00E+00		2.787	445	1.17E-01
S5	3.024	410	4.93E-02		2.822	439	1.11E+00
S6	3.050	406	0.00E+00		2.900	427	3.50E-01
S7	3.167	391	1.17E-01		2.999	413	3.21E-01
S8	3.225	384	0.00E+00		3.062	405	1.86E-02
S9	3.275	379	1.50E-01		3.074	403	6.35E-04
S10	3.297	376	4.61E-03		3.145	394	4.86E-03
S11	3.304	375	0.00E+00		3.230	384	4.70E-02
S12	3.319	374	0.00E+00		3.257	381	1.80E-02

S13	3.326	373	1.21E-02		3.279	378	2.38E-02
S14	3.340	371	0.00E+00		3.321	373	7.98E-02
S15	3.644	340	1.52E-02		3.533	351	3.38E-02
S16	3.681	337	0.00E+00		3.591	345	2.52E-03
S17	3.697	335	8.52E-02		3.618	343	9.57E-03
S18	3.743	331	0.00E+00		3.643	340	7.72E-03
S19	3.762	330	7.13E-03		3.659	339	3.72E-03
S20	3.766	329	2.81E-02		3.680	337	3.25E-03
S21	3.769	329	0.00E+00		3.688	336	1.04E-02
S22	3.786	327	0.00E+00		3.700	335	3.48E-03
S23	3.809	325	7.22E-03		3.708	334	3.94E-03
S24	3.811	325	9.84E-02		3.718	333	1.51E-02
S25	3.831	324	0.00E+00		3.727	333	1.12E-03
S26	3.843	323	7.51E-02		3.730	332	6.42E-03
S27	3.843	323	0.00E+00		3.745	331	5.06E-02
S28	3.863	321	0.00E+00		3.761	330	9.81E-03
S29	3.874	320	2.10E-02		3.766	329	4.55E-02
S30	3.895	318	0.00E+00		3.771	329	1.22E-02
S31	3.909	317	7.70E-04		3.787	327	1.91E-02
S32	3.923	316	0.00E+00		3.792	327	4.40E-02
S33	3.928	316	2.43E-01		3.803	326	5.37E-03
S34	3.937	315	0.00E+00		3.810	325	2.36E-02
S35	3.946	314	0.00E+00		3.822	324	5.70E-02
S36	3.955	314	1.06E-02		3.836	323	3.58E-02
S37	3.983	311	5.17E-03		3.854	322	1.16E-03
S38	3.991	311	0.00E+00		3.871	320	1.32E-03
S39	3.992	311	0.00E+00		3.902	318	1.62E-03
S40	4.002	310	3.76E-02		3.910	317	8.18E-03
S41	4.014	309	9.43E-02		3.916	317	1.05E-02
S42	4.016	309	0.00E+00		3.931	315	1.06E-02
S43	4.021	308	0.00E+00		3.938	315	2.13E-02
S44	4.025	308	2.98E-02		3.949	314	9.65E-02
S45	4.056	306	0.00E+00		3.957	313	5.80E-02
S46	4.058	305	5.09E-02		3.972	312	9.99E-03
S47	4.068	305	6.37E-02		3.991	311	3.69E-03
S48	4.073	304	0.00E+00		4.018	309	7.52E-03
S49	4.089	303	1.38E-01		4.020	308	7.12E-03
S50	4.127	300	9.64E-02		4.021	308	1.44E-02

Table S15. Distortion (E_{dist}), emission (E_{em}) and stabilization (E_{stab}) energies, difference in stabilization energies (ΔE_{stab}) and emission wavelength (λ_{em}) for the different triplet states computed for **L1** and the **Cu-NIR1** and **Cu-NIR1** complexes. For comparison the absorption energy computed at Franck-Condon geometry (E_{abs}) of the ^{3}MLCT state is provided. Energies and wavelengths are given in [eV] and [nm], respectively.

	L1	Cu-NIR1		Cu-NIR2	
	S_1	T_{1a}	T_{1b}	T_{1a}	T_{1b}
character	^{1}LC	^{3}MLCT	^{3}LC	^{3}MLCT	^{3}LC
E_{abs}		2.236		2.203	
E_{dist}		0.527	0.439	0.599	0.456
E_{em}		1.322	1.541	1.299	1.478
E_{stab}		1.849	1.980	1.898	1.934
ΔE_{stab}		0.000	0.131	0.000	0.035
λ_{em}	511	938	805	954	839

Table S16. Summary of the EL characteristics of the LECs based on complex **Cu-NIR1**, **Cu-NIR2**, **M1**, and **M2** (80 wt.%) and [BMIM$^+$(PF$_6$)$^-$] (20 wt.%).

Complex	Concentration (mg mL^{-1}) [a]	Thickness (nm)	Bias (V)	EL$_{max}$ (nm) [b]	L$_{max}$ (μW cm^{-2}) [c]	$\eta_{ext, max}$ (%) [d]	$\eta_{P, max}$ (mW W^{-1}) [e]
	40	84	4	668	5.39	0.22	1.00
Cu-NIR1	60	151	5	747	7.48	0.32	1.07
	80	289	6	714	5.73	0.31	0.89
	40	73	7	656	5.01	0.07	0.18
Cu-NIR2	60	160	8	733	5.65	0.17	0.37
	80	278	8	670	1.10	0.14	0.32
M1	70	151	4.5	666-716	12.09	0.53	2.19
M2	60	159	3.2	664	2.99	0.54	3.08

[a] Solution concentration for spin coating. [b] Stabilized EL emission peak wavelength. [c] Maximal light output power. [d] Maximal external quantum efficiency. [e] Power efficiency.